

The Galaxy and its stellar halo: insights on their formation from a hybrid cosmological approach

Gabriella De Lucia^{1*} and Amina Helmi²

¹*Max-Planck-Institut für Astrophysik, Karl-Schwarzschild-Str. 1, D-85748 Garching, Germany*

²*Kapteyn Astronomical Institute, University of Groningen, P.O. Box 800, 9700 AV Groningen, Netherlands*

22 October 2018

ABSTRACT

We use a series of high-resolution simulations of a ‘Milky-Way’ halo coupled to semi-analytic methods to study the formation of our own Galaxy and of its stellar halo. The physical properties of our model Milky Way, as well as the age and metallicity distribution of stars in the different components, are in relatively good agreement with observational measurements. Assuming that the stellar halo builds up from the cores of the satellite galaxies that merged with the Milky Way over its life-time, we are able to study the physical and structural properties of this component. In agreement with previous work, we find that the largest contribution to the stellar halo should come from a few relatively massive ($10^8 - 10^{10} M_{\odot}$) satellites, accreted at early times. Our “stellar halo” does not exhibit any clear metallicity gradient, but higher metallicity stars are more centrally concentrated than stars of lower abundance. This indicates that the probability of observing low-metallicity halo stars increases with distance from the Galactic centre. We find that the proposed “dual” nature of the Galactic stellar halo can be explained in our model as a result of a mass-metallicity relation imprinted in the building blocks of this component.

Key words: Galaxy: formation – Galaxy: evolution – Galaxy: stellar content – Galaxy: halo

1 INTRODUCTION

Our own galaxy - the Milky Way - is a fairly large spiral galaxy consisting of four main stellar components. Most of the stars are distributed in a thin disk, exhibit a wide range of ages, and are on high angular momentum orbits. A much smaller mass of stars (about 10-20 per cent of that in the thin disk) reside in a distinct component which was established about 25 years ago though star counts (Gilmore & Reid 1983), and which is referred to as the ‘thick disk’. The stars in the thick disk are old, have on average lower metallicity than those of similar age in the thin disk, and are on orbits of lower angular momentum. The Galactic bulge is dominated by an old and relatively metal-rich stellar population with a tail to low abundances. It has a peanut-shape (Dwek et al. 1995), is kinematically hotter than the Milky Way disk but colder than the Milky Way halo (Kuijken & Rich 2002). The stellar halo represents only a tiny fraction of the total stellar mass ($\sim 2 \times 10^9 M_{\odot}$ - Carney, Latham & Laird 1989), and is dominated by old and metal poor stars which reside on low angular momentum orbits.

While the Milky Way is only one galaxy, it is the one

that we can study in unique detail. Accurate measurements of ages, metallicities, and kinematics have been collected over the years for a large number of individual stars. Over the next decade, a number of astrometric and spectroscopic surveys will provide accurate spatial, kinematic, and chemical information for a much larger number of stars (e.g. the satellite *Gaia* - Perryman et al. 2001; the Radial Velocity Experiment *RAVE* - Steinmetz et al. 2006; and the Sloan Extension for Galactic Understanding and Exploration *SEGUE* - Beers et al. 2004). This vast amount of fossil information will provide important advances in our understanding of the sequence of events which led to the formation of our Galaxy (Freeman & Bland-Hawthorn 2002).

Historically, chemical and kinematic information were used as a basis to formulate the first galaxy formation models. In their classical paper, Eggen, Lynden-Bell & Sandage (1962) analysed the properties and motion of 221 dwarfs and showed that those of lower metallicity tended to move on more highly eccentric orbits. The observed trends were interpreted as a signature that the stars now observed as a spheroidal halo formed during a rapid radial collapse that later continued to form the stellar disk. About one decade later, Searle & Zinn (1978) measured the metallicities in a sample of globular clusters and found no signifi-

* Email: gdelucia@mpa-garching.mpg.de

cant abundance gradient as a function of the galactocentric distance. These observations led Searle & Zinn to formulate the hypothesis that the stellar halo formed over a longer timescale through agglomeration of many sub-galactic ‘fragments’ that may be similar to the surviving dwarf spheroidal galaxies today observed as satellites of the Milky Way. The observational evidence in support of this scenario has mounted significantly in the last decade ranging from detection of significant clumpiness in the phase space distribution of halo and disk stars (e.g. Majewski, Munn & Hawley 1996; Helmi et al. 1999; Chiba & Beers 2000; Helmi et al. 2006) to the direct detection of satellite galaxies caught in the act of tidal disruption (e.g. Ibata, Gilmore & Irwin 1994; Martin et al. 2004; Zucker et al. 2006).

The Searle & Zinn scenario, and the observational results mentioned above, are in qualitative agreement with expectations from the hierarchical cold dark matter (CDM) model which, with the ‘concordance’ set of cosmological parameters (Λ CDM), boasts a considerable degree of success in reproducing a large number of observations at various cosmic epochs, in particular on large scales. On galactic and sub-galactic scales, the success of the model has not been convincingly demonstrated yet, and a number of issues remain subject of a lively debate in the astronomical community. Among these are the dwarf galaxy counts, the degree of concentration of dark matter haloes, and the rotation curves of dwarfs and low surface brightness galaxies (e.g. Simon et al. 2003; Kazantzidis et al. 2004; Stoehr 2006; Strigari et al. 2007, and references therein).

The origin and structure of the stellar halo has been studied by several authors, using a variety of techniques (for a review, see Helmi 2008). These include cosmological numerical simulations with and without baryonic physics (e.g. Diemand, Madau & Moore 2005; Abadi, Navarro & Steinmetz 2006), and phenomenological modelling of the evolution of baryons inside haloes, usually in combination with N-body simulations that provide the dynamical history of the system (Bullock & Johnston 2005).

A number of recent studies have raised concerns about the Searle & Zinn scenario on the basis of the observation that stars in Local Group dwarf spheroidals (dSph’s) tend to have lower α abundances than stars in the stellar halo (Shetrone et al. 2001; Tolstoy et al. 2003; Venn et al. 2004). The observed abundance pattern excludes the possibility that a significant contribution to the stellar halo comes from disrupted satellites similar to the *present day* dSph’s. It is not entirely unexpected that the surviving satellites might be intrinsically different from the main contributors to the stellar halo, given they had a Hubble time to evolve as independent entities. This argument has been put forward in a recent series of papers by Bullock & Johnston (2005), Robertson et al. (2005), and Font et al. (2006) who reproduce the observed chemical abundance pattern by combining mass accretion histories of galaxy-size haloes with a chemical evolution model for individual satellites. In their model, the agreement with the observed trends is a consequence of the fact that the stellar halo originates from a few (relatively massive) satellites accreted early on and enriched in α -elements by type II supernovae. The surviving satellites are typically accreted much later, have more extended star formation histories and stellar populations enriched to solar level by both type II and type Ia supernovae. A more serious

problem with the Searle & Zinn scenario has been pointed out by Helmi et al. (2006) who found a significant difference between the metal-poor tail of the dSph metallicity distribution and that of the Galactic halo, demonstrating that the progenitors of present day dSph’s are fundamentally different from the building blocks of our Galaxy, even at earliest epochs. One possible solution discussed in Helmi et al. is that the Galactic building blocks formed from the collapse of high- σ density fluctuations in the early Universe, while the present day satellites would originate from low- σ peaks (see also Salvadori, Ferrara & Schneider 2008).

The formation and the evolution of the baryonic component of galaxies is regulated by a number of non-linear processes operating on vastly different scales (e.g. shocking and cooling of gas, star formation, feedback by supernovae and active galactic nuclei, chemical enrichment, and stellar evolution). Most of these processes are quite poorly understood even when viewed in isolation. The difficulties grow considerably when one takes into account the fact that the physical properties of galaxies are determined by a complex network of actions, back-reactions, and self-regulation between the above mentioned physical processes. In recent years, different approaches have been developed to link the observed properties of luminous galaxies to the dark matter haloes within which they reside. Among these, semi-analytic models have developed into a powerful and widely used tool to study galaxy formation in the framework of the currently standard model for structure formation. In these models, the evolution of the baryonic component is modelled invoking ‘simple’, yet physically and observationally motivated ‘prescriptions’. These techniques find their seeds in the pioneering work by White & Rees (1978); they have been laid out in a more detailed form in the early 90s (White & Frenk 1991; Cole 1991; Kauffmann, White & Guiderdoni 1993) and have been substantially extended and refined in the last years by a number of different groups. Modern semi-analytic models of galaxy formation take advantage of high resolution N-body simulations to specify the location and evolution of dark matter haloes - which are assumed to be the birthplaces of luminous galaxies (Kauffmann et al. 1999; Benson et al. 2000; Springel et al. 2001; Hatton et al. 2003). Using this ‘hybrid’ approach, it is possible not only to predict observable physical properties such as luminosities, metallicities, star formation rates, etc., but also to provide full spatial and kinematical information of model galaxies thus allowing more accurate and straightforward comparisons with observational data to be carried out. In this paper, we use this hybrid approach to study the formation of the Milky Way galaxy and of its stellar halo.

The numerical simulations used in our study are described in Sec 2, while in Sec. 3 we give a brief introduction to the adopted semi-analytic technique, and details of the specific model used in our study. In Sec. 4, we compare model results to the observed properties of the Milky Way, and discuss their dependence on a number of model parameters. In Sec. 5, we study the age and metallicity distribution of the spheroid and disk components of our model Galaxy. In Sec. 6, we analyse the formation and structure of the stellar halo. We discuss and summarise our results, and give our conclusions in Sec. 7.

Table 1. Numerical parameters of the re-simulations used in this study. In the table, we give the particle mass m_p , the number of particles, the starting redshift z_{start} , and the gravitational softening ϵ . All these quantities refer to the particles in the high resolution region only.

Name	$m_p [h^{-1}M_\odot]$	N_{HR}	z_{start}	$\epsilon [h^{-1}\text{kpc}]$
GA0	1.677×10^8	68323	70	1.4
GA1	1.796×10^7	637966	80	0.8
GA2	1.925×10^6	5953033	90	0.38
GA3	2.063×10^5	55564205	60	0.18

2 THE SIMULATIONS

In this paper, we use the re-simulations of a ‘Milky Way’ halo (the GA series) described in Stoehr et al. (2002) and Stoehr et al. (2003). The underlying cosmological model is a flat Λ -dominated CDM Universe with cosmological parameters: $\Omega_m = 0.3$, $\Omega_\Lambda = 0.7$, $H_0 = 70 \text{ km s}^{-1} \text{ Mpc}^{-1}$, $n = 1$, and $\sigma_8 = 0.9$. The simulations were generated using the ‘zoom’ technique (Tormen, Bouchet & White 1997) starting from an intermediate-resolution simulation (particle mass $\sim 10^8 M_\odot$) of a ‘typical’ region of the Universe. A ‘Milky Way’ halo was selected as a relatively isolated halo which suffered its last major merger at $z > 2$, and with approximately the correct peak rotation velocity. These choices were intended to select a candidate for resimulations with properties that closely match the observed ones: our Galaxy is believed to have had a quiet merging history, with the last major merging event occurring some 10-12 Gyr ago (Gilmore et al. 2002), and it is a quite isolated galaxy with the closest cluster (Virgo) lying at a distance of about 20 Mpc.

It is important to note that haloes with such quiet merging histories are not uncommon in Λ CDM cosmologies. Using the Millennium Simulation (Springel et al. 2005), we determined the epoch of the last accretion event corresponding to an increase in mass of the main progenitor of a factor ~ 0.3 (i.e. a ‘major merger’) for haloes with present-day mass in the range 1 to $3 \times 10^{12} M_\odot$. We find that about 57 per cent of these haloes experienced their last ‘major merger’ at redshift larger than 2. The estimated fraction should be considered as an upper limit, as part of the accretion might occur through diffuse material. Lower - but still significant - fractions (about 45 per cent) have been found in a recent analysis by Stewart et al. (2007), and in other independent studies (Boylan-Kolchin, private communication).

The selected halo was then re-simulated at a series of four progressively higher resolution simulations using the code GADGET (Springel, Yoshida & White 2001). The numerical parameters used in the high resolution regions of these re-simulations are summarised in Table 1.

Simulation data were stored in 108 outputs from $z = 37.6$ to $z = 0$. These are approximately logarithmically spaced in time down to $z = 2.3$, and approximately linearly spaced in time thereafter. For each simulation snapshot, we constructed group catalogues using a standard friends-of-friends (FOF) algorithm with a linking length of 0.2 in units of the mean particle separation. Each group was then decomposed into a set of disjoint substructures using the algorithm SUBFIND (Springel et al. 2001). As in previous work,

Table 2. M_{200} and V_{max} for the four simulations used in this study.

Name	$M_{200} [M_\odot]$	$V_{\text{max}} [\text{km s}^{-1}]$
GA0	3.35×10^{12}	250.71
GA1	3.28×10^{12}	246.60
GA2	3.21×10^{12}	247.05
GA3	2.98×10^{12}	251.20

we consider to be genuine substructures only those with at least 20 bound particles which sets the subhalo detection limit to 4.79×10^9 , 5.13×10^8 , 5.5×10^7 , and $5.89 \times 10^6 M_\odot$ for the four simulations used in our study. Substructure catalogues were then used to construct merger history trees for all self-bound haloes as described in detail in Springel et al. (2005) and De Lucia & Blaizot (2007). We recall that the merger tree construction is based on the determination of a unique descendant for any given halo. In order to determine the appropriate descendant, for each halo we find all haloes in the following snapshot that contain its particles, and then count the particles giving higher weight to those that are more tightly bound in the halo under consideration. As a reference, Springel et al. (2005) gave about three times more weight to the half most bound particles of a halo of 100 particles. (The relative weight of the half most bound particles increases with particle number.) For our analysis, we are interested in tracing well the cores of the accreted satellites (see Sec. 6), and we noted that the tree construction adopted in previous work lead to occasional premature mergers. In order to avoid these events, we have slightly increased the weight of the most bound particles (four times more weight is given to the half most bound particles of a 100 particle halo). The merger trees constructed as described above, represent the basic input needed for the semi-analytic model which is described in the next section.

In Table 2, we list the masses (M_{200}) and maximum velocities for the main halo in the four simulations used in this study.¹ Latest observational results give $V_{\text{max}} \sim 180 - 220 \text{ km s}^{-1}$ and a mass $M_{\text{MW}} \sim 1 \times 10^{12} M_\odot$ (Battaglia et al. 2005; Smith et al. 2007). Our simulated haloes therefore appear more massive than the Milky-Way halo. Following Helmi et al. (2003), we scale our simulations to a ‘Milky Way’ halo by adopting a scaling factor in mass $M_{200}/M_{\text{MW}} = \gamma^3 = 2.86$. This implies that we scale down the positions and velocities by the same factor $\gamma = 1.42$ in all four simulations.

Fig. 1 shows the projected density distribution of the dark matter for the simulation GA3, at six different redshifts. The box at $z = 0$ is centred on the most bound particle of the GA3 halo, while those at higher redshift are centred on the most bound particle of the main progenitor of the GA3 halo at the corresponding redshift.

¹ M_{200} is defined here as the mass within a sphere of density 200 times the critical density.

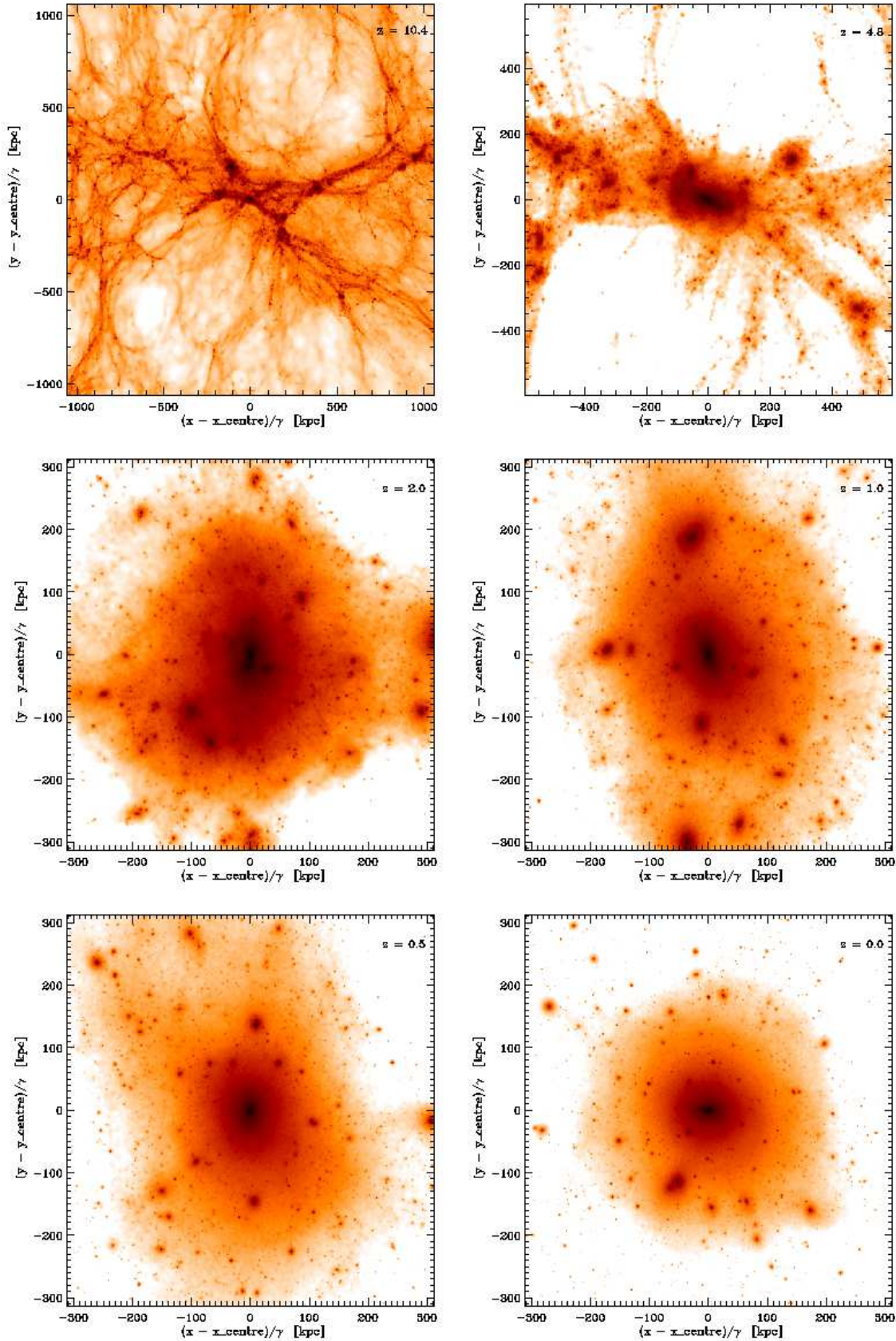


Figure 1. Projected density distribution of the dark matter for the simulation GA3, at six different redshifts (from top left to bottom right: 10.4, 4.8, 2.0, 1.0, 0.5, and 0). The box at $z = 0$ is centred on the most bound particle of the GA3 halo, while those at higher redshift are centred on the most bound particle of the main progenitor of the GA3 halo at the corresponding redshift. For all panels, the depth of the box is 500 kpc comoving. As explained in the text, positions are scaled by a factor $\gamma = 1.42$.

3 THE HYBRID MODEL OF GALAXY FORMATION

A complete review of semi-analytic techniques goes beyond the scope of this paper. For a pedagogical and historical introduction to semi-analytic methods, we refer the interested reader to the recent review by Baugh (2006). In this section, we briefly summarise how a semi-analytic model is grafted onto high resolution N -body simulations, and give a brief account of those aspects of the physical model which are relevant for the present study.

The basic assumption is that galaxies form when gas condenses at the centre of dark matter haloes. Star formation, feedback processes, chemical enrichment, etc. take then place according to analytical laws which are based on theoretical and/or observational arguments. Adopting this formalism, it is possible to express the full process of galaxy evolution through a set of differential equations that describe the variation in mass as a function of time of the different galactic components (e.g. stars, gas, metals), and that are coupled to the merger history of the dark matter haloes extracted from the N -body simulations (e.g. see Fig. 1 and Sec. 4.7 in De Lucia, Kauffmann & White 2004). Given our limited understanding of the physical processes that regulate galaxy formation and evolution, the equations describing these processes contain ‘free’ parameters whose value is typically chosen in order to provide a reasonably good agreement with the observational data in the local Universe.

The semi-analytic model used in this study builds on the methodology originally introduced by Springel et al. (2001) and De Lucia et al. (2004), and has been recently updated to include a model for the suppression of cooling flows by ‘radio-mode’ AGN feedback as described in detail in Croton et al. (2006). Details about the modelling adopted for the various physical processes considered can be found in Croton et al. (2006) and De Lucia & Blaizot (2007).

We recall that our approach follows explicitly dark matter haloes when they are accreted into larger systems. This allows the dynamics of satellite galaxies residing in the infalling haloes to be properly followed until their parent dark matter substructures are completely destroyed by tidal truncation and stripping (Ghigna et al. 2000; De Lucia et al. 2004; Gao et al. 2004). When this happens, the satellite galaxy residing at the centre of the substructure under consideration is assumed to merge onto the central galaxy after a residual surviving time that is estimated from the relative orbit of the two merging objects, at the time of subhalo disruption:

$$T_{\text{merge}} = 1.17 \cdot f_{\text{fudge}} \cdot \frac{r_{\text{sat}}^2 \cdot V_{\text{virial}}}{\ln \Lambda \cdot G \cdot M_{\text{sat}}}$$

In the above equation, M_{sat} is the mass of the substructure at the last time it is identified, r_{sat} is the distance between the merging halo and the centre of the structure on which it is accreted, V_{virial} is the virial velocity of the accreting structure, and we approximate the Coulomb logarithm with $\ln \Lambda = (1 + M_{\text{vir}}/M_{\text{sat}})$. We therefore allow the satellite galaxy to further sink in through dynamical friction, even after its dark matter halo has fallen below the resolution limit of our simulations. When a halo is accreted onto a larger structure, its mass is reduced by tidal stripping and its orbit is shrunk by dynamical friction, until the

substructure can no longer be identified as a self-bound overdensity orbiting the smooth dark matter background of the larger system. This ‘disruption’ of the dark matter substructure typically occurs at $r_{\text{sat}} \geq 0.1R_{\text{vir}}$ which can be much larger than the separation from which the galaxy merger is expected to happen. We note, finally, that previous work has shown that this treatment of orphan galaxies is required in order to reproduce the correlation signal at small scales (Wang et al. 2006; Kitzbichler & White 2008).

Mild variations of the above formula are used in different semi-analytic models with differences entering mainly the way each model treats the orbital distribution, $\ln \Lambda$, and f_{fudge} (see discussion in Boylan-Kolchin, Ma & Quataert 2008). In this work, we have followed De Lucia & Blaizot (2007) and used $f_{\text{fudge}} = 2$, which is in better agreement with recent numerical work indicating that the classical dynamical friction formulation tends to underestimate the merging times measured from simulations (Boylan-Kolchin et al. 2008; Jiang et al. 2008). Results of these studies, however, are still quantitatively different and additional work is needed in order to calibrate the correct pre-factor and/or corrections to apply to the classical formula.

The stellar mass of the satellite galaxies is assumed to be unaffected by the tidal stripping process that reduces the mass of its parent halo. However, such tidal effects may well dominate the disruption process of satellites orbiting in a galaxy halo (Peñarrubia & Benson 2005). Therefore, our implementation could lead to an underestimate of the stellar mass in diffuse form, and to an overestimate of the number and/or luminosity of satellite galaxies. We will see however, that this does not affect our conclusions in any significant way.

As in previous work (Croton et al. 2006; De Lucia et al. 2006), we assume that spheroid formation occurs through both mergers and disk instability. In the case of a ‘minor’ merger, we transfer the stellar mass of the merged galaxy to the spheroid of the central galaxy. The cold gas of the satellite galaxy is added to the disk of the central galaxy, and a fraction of the combined cold gas from both galaxies is turned into stars as a result of the merger. Any stars that formed during the burst are also added to the disk of the central galaxy. The photometric properties of the galaxy are updated accordingly using the same method described in De Lucia et al. (2004). If the mass ratio of the merging galaxies is larger than 0.3, we assume that we witness a ‘major’ merger that gives rise to a more significant starburst and destroys the disk of the central galaxy completely, leaving a purely spheroidal stellar remnant. The galaxy can grow a new disk later on, provided it is fed by an appreciable cooling flow. Note that the modelled spheroidal component includes both the bulge and the stellar halo.

Following Mo, Mao & White (1998), we assume that a stellar disk becomes unstable when the following condition is verified:

$$\frac{V_{\text{max}}}{(G m_{\text{disk}}/r_{\text{disk}})^{1/2}} \lesssim 1.1$$

This condition is based on the numerical work by Efstathiou, Lake & Negroponte (1982) who used N -body simulations to investigate the development of global instabilities in exponential disks embedded in a variety of haloes.

In this work, we assume that each time a galaxy meets the above criterion, a fixed fraction (F_{inst}) of the stellar mass in the disk is transferred to the central spheroid component. The instability criterion is applied only to disk dominated systems ($M_{\text{spheroid}}/M_{\text{tot}} < 0.1$). This choice is motivated by numerical studies that showed that a spheroid component can stabilise the disk against bar formation, giving the galaxy an inner Lindblad resonance which does not allow swing amplification of waves through the centre (e.g. Sellwood 1989; Sellwood & Moore 1999). The parameter F_{inst} is chosen so as to get a morphological mix that is in reasonable agreement with the observational measurements for the local Universe², and is assumed to be equal to 0.5. We note that, according to the condition above, the occurrence of disk instability episodes follows essentially from the way the disk mass builds up relative to the total mass of the halo, and that the condition $M_{\text{spheroid}}/M_{\text{tot}} < 0.1$ efficiently suppresses the occurrence of late instability episodes even in galaxies with modest bulge-to-total ratios.

Admittedly, our modelling of disk instability is very simplified, and gives a very crude description of the complex phenomenology associated to bar formation and evolution, which is the subject of current active research (Martinez-Valpuesta et al. 2006; Berentzen et al. 2007; Curir et al. 2007, and references therein). We are, for example, neglecting the possibility that bar formation produces an inflow of gas towards the centre that could fuel starburst/AGN activity, and that can eventually lead to bar disruption. In addition, present simulations do not provide clear indications about the fraction of disk mass that gets redistributed and how this depends on the halo/galaxy properties. We therefore consider the results of our simple modelling as just indicative and, in the following, we also comment on results obtained when the disk instability channel for bulge formation is switched off.

In this paper, we adopt an improved model to estimate the disk radii. Assuming conservation of specific angular momentum, we assume that when hot gas cools at the centre of dark matter haloes, it settles in a rotationally supported disk with exponential scale-length given by:

$$r_D = \frac{\lambda}{\sqrt{2}} R_{200}$$

where λ is the halo spin parameter (Mo et al. 1998). Following Hatton et al. (2003), we recompute the scale-length at each time-step by taking the mass-weighted average gas profile of the disk and that of the new material being accreted. The scale-length of the disk is not altered after a galaxy becomes a satellite.

As in previous work, we assume that the star formation occurs at a rate given by:

$$\psi = \alpha_{\text{SF}} M_{\text{sf}} / t_{\text{dyn}}$$

where $t_{\text{dyn}} = r_{\text{disk}}/V_{\text{vir}}$ is the dynamical time of the galaxy and we assume that the star forming region (r_{disk}) extends to about $3 \times r_D$. The parameter α_{SF} regulates the efficiency of the conversion of gas into stars, and M_{sf} represents the amount of gas available for star formation which can be expressed as:

$$M_{\text{sf}} = 2\pi \int_0^{r_{\text{crit}}} \Sigma_D(r) r dr$$

where r_{crit} is the radius at which the gas surface density drops below the following critical value (Kennicutt 1989):

$$\Sigma_{\text{crit}} [M_{\odot} \text{pc}^{-2}] = 0.59 V [\text{kms}^{-1}] / r_{\text{disk}} [\text{kpc}].$$

For a complete summary of the model parameters adopted in our fiducial model, we refer to Table 1 of Croton et al. (2006). As explained in De Lucia & Blaizot (2007), the adoption of a Chabrier Initial Mass Function led to slight modifications of some of these parameters. We refer to these papers for more details about the parametrisation adopted for the various physical processes explicitly taken into account in our model, and for a complete characterisation of model parameters.

4 DEPENDENCY ON MODEL PARAMETERS AND NUMERICAL RESOLUTION

In order to provide an illustration of how model results are affected by different choices of model parameters, we show in Fig. 2 how different physical properties of our model Milky Way galaxy vary on a limited model grid where we have altered only the values of the star formation and supernovae feedback efficiencies. These correspond to the parameters “ α_{SF} ” and “ ϵ_{disk} ” in Table 1 of Croton et al. (2006), and regulate the amount of cold gas that is converted into stars in a disk dynamical time, and the amount of cold gas reheated by supernovae explosions. As explained in the previous section, our fiducial model uses the same combination of model parameters adopted in De Lucia & Blaizot (2007), and is indicated by the vertical solid line in Fig. 2.

In the figure, different colours for filled circles correspond to different values for the star formation efficiency parameter: 0.03 (red), 0.08 (green), 0.13 (blue). Different colours for open circles correspond to different values for the SN feedback efficiency: 1.5 (green), 3.5 (red), 5.5 (blue). Red horizontal lines in each panel indicate the observational measurements. Fig. 2 shows results from our highest resolution simulation (GA3), but similar trends are obtained for the lower resolution simulations used in this study (see below).

Increasing α_{SF} (red, green, blue filled circles) and keeping ϵ_{disk} constant (open circles of the same colour) produces an increase of total mass, and a corresponding decrease in of the amount of cold gas available. As explained in De Lucia et al. (2004), metals are exchanged between different components proportionally to the exchanged mass so that the increase in mass is reflected in a parallel increase in the amount of metals (bottom left panel in Fig. 2). The mass of the spheroid component (top left panel) varies in a non-monotonic way with increasing star formation efficiency because disk instability episodes (see previous section) occur at different times. In our model, black holes grow primarily during mergers, both by merging with each other and by accretion of cold gas (see Sec. 3.4 of Croton et al. 2006). The black hole mass therefore decreases with increasing star formation efficiency (middle left panel) as a consequence of the decrease of the cold gas available.

Increasing ϵ_{disk} (green, red, blue open circles) and keeping α_{SF} constant (filled circles of the same colour), the final

² The morphological mix resulting from the adopted model has been computed for the Millennium Simulation.

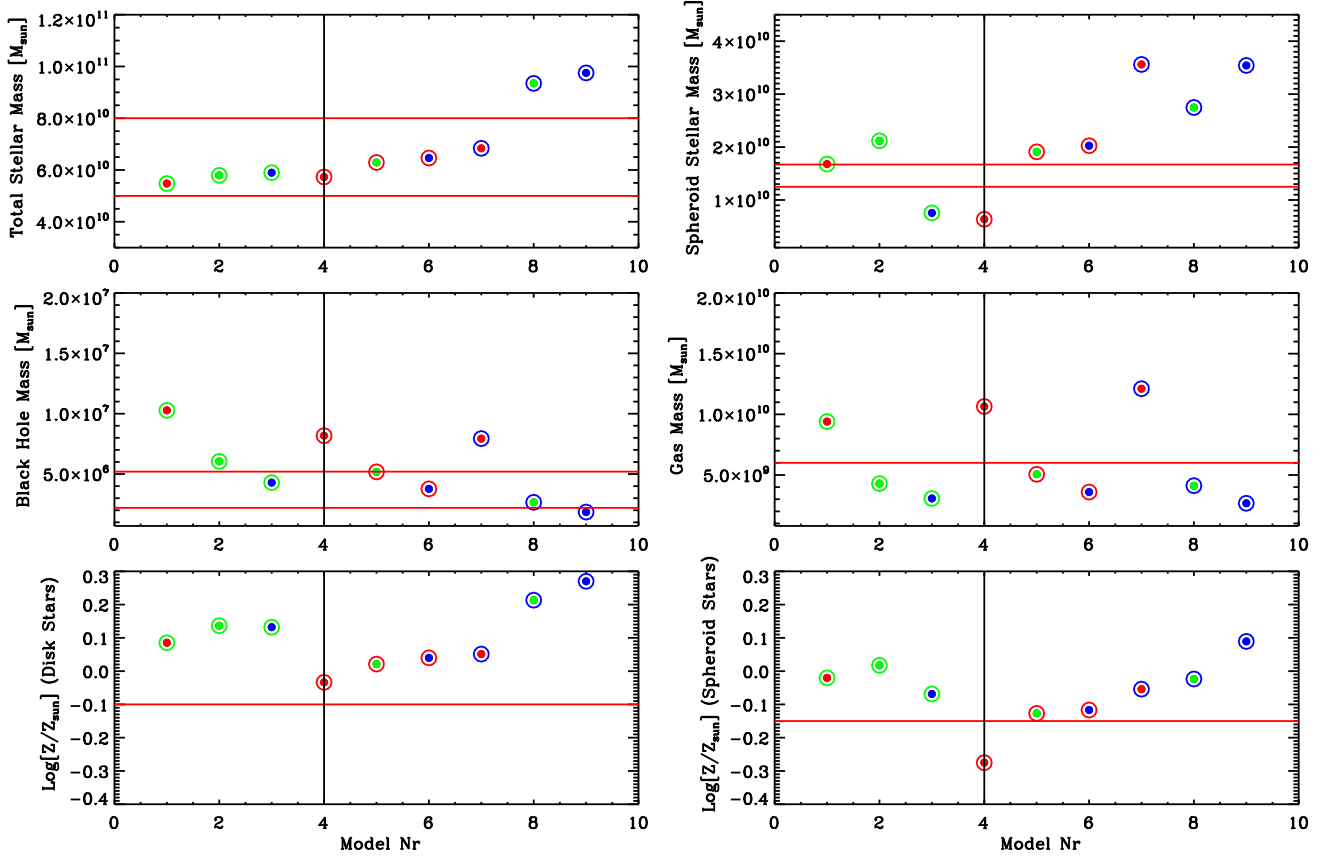


Figure 2. Physical properties of our model Milky Way galaxy from the simulation GA3, as a function of different combinations of the star formation efficiency (α_{SF}), and of the supernovae feedback efficiency (ϵ_{disk}). Different colours for filled circles correspond to different values for the star formation efficiency parameter: 0.03 (red), 0.08 (green), 0.13 (blue). Different colours for open circles correspond to different values for the SN feedback efficiency: 1.5 (green), 3.5 (red), 5.5 (blue). The vertical black line (corresponding to model number 4) indicates our fiducial model. Red horizontal lines in each panel indicate observational estimates. Note that in the bottom right panel we compare the metallicity of the spheroid in our models to that of the Galactic bulge.

amount of gas stays almost constant because gas ejected by satellite galaxies is rapidly re-incorporated³, and because the higher level of enrichment of the hot gas component causes a more efficient cooling. As a consequence, the total stellar mass increases (top left panel), and the black hole mass decreases slightly (middle left panel).

For our reference model, the total stellar mass is $\sim 6 \times 10^{10} M_{\odot}$, in very good agreement with the estimated value of $\sim 5 - 8 \times 10^{10} M_{\odot}$. The mass of the spheroidal component is instead slightly lower than the observed value (assumed to be ~ 25 per cent of the disk stellar mass, or $1.25 - 1.6 \times 10^{10} M_{\odot}$ - Bissantz et al. 2004). Studying the proper motion of Galactic Centre stars, Schödel et al. (2002) estimated a central point mass of $(3.7 \pm 1.5) \times 10^6 M_{\odot}$, which is lower than the value obtained for our Milky Way

in the reference model. This is not surprising given that our model for the formation of black holes was tuned to match the local relation between black hole mass and bulge mass (Croton et al. 2006), and that the value measured for the Milky Way is offset from this relation. The total mass of H_2 in the Milky Way galaxy is $\sim 1 \times 10^9 M_{\odot}$ and the total mass of HI gas is $\sim 5 \times 10^9 M_{\odot}$ (Blitz 1997, and references therein). Fig. 2 shows that our fiducial model gives a gas mass which is about twice the estimated value, and that this ‘problem’ could be alleviated by increasing the star formation efficiency. The stars of the Galactic bulge are found to peak at near solar value ($[Fe/H] \sim -0.15$), with a relatively wide spread, while the stars in the disk have $[Fe/H] \sim -0.1$ (Freeman & Bland-Hawthorn 2002, see also Sec. 5). The corresponding metallicities for the galaxy in the reference model are not far from the observed values. Note, however, that the metallicities shown in Fig. 2, and in the rest of this paper, refer to total metallicities (and not only to $[Fe/H]$). It should be stressed that our model assumes an instantaneous recycling approximation, i.e. we neglect the delay between star formation and the recycling of gas and metals from stellar winds and supernovae. The model is therefore not able to

³ Following De Lucia et al. (2004), we assume that the material that is ejected outside the haloes as a consequence of supernovae explosions, can be re-incorporated into the hot gas component after a time-scale that is proportional to the dynamical time-scale of the halo. Our default model adopts the same re-incorporation efficiency as in Croton et al. (2006).

take into account the evolution of different element abundances, and in particular it does not describe well the elements around the iron-peak, which are mainly produced by supernovae Ia and which typically return their products on longer timescales. We will come back to this issue later.

Overall, Fig. 2 demonstrates that our reference model is in relatively good agreement with observational measurements (although there are other combinations of model parameters that also provide a reasonable agreement). This is not entirely surprising given that model parameters are tuned to reproduce the local galaxy luminosity function *and* the mass and luminosity of ‘Milky-Way’ galaxies (see De Lucia et al. 2004). In previous work, we have shown that our fiducial model is in quite good agreement with the observed relations between stellar mass, gas mass, and metallicity (De Lucia et al. 2004), the observed luminosity, colour, and morphology distributions (Croton et al. 2006; De Lucia et al. 2006), and the observed two-point correlation functions (Springel et al. 2005; Wang et al. 2007). Kitzbichler & White (2007) have recently shown that it also agrees reasonably well with the observed galaxy luminosity and mass functions at higher redshift. In the following, we will therefore focus on results from our fiducial model. It is worth mentioning at this point that our default model, which assumes a redshift of reionization $z \sim 7$ (Croton et al. 2006), over-predicts the number of observed satellites. The situation is significantly improved when adopting an earlier epoch of reionization which does not affect significantly the model Galaxy and the results presented in this paper. We will present a more detailed analysis of the satellite population for our model Milky Way in a forthcoming paper.

Fig. 3 shows the evolution of different mass and metallicity components for the model Milky Way galaxies in the four simulations used in this study (lines of different colours). The histories shown in panels (a) to (f) are obtained by tracking the evolution of the ‘main progenitor’, which is obtained by linking the galaxy at each time-step to the progenitor with the largest stellar mass. For our model Milky Way, the galaxies merging onto the main branch have stellar masses that are much smaller than the current mass of the main progenitor, over most of the galaxy’s life-time, explaining the smooth increase of the stellar mass component. In these cases, the main progenitor branch does indeed provide a quite good approximation of the evolution of the galaxy itself (see discussion in De Lucia & Blaizot 2007).

Fig. 3 shows that approximately half of the final mass in the dark matter halo is already in place (in the main progenitor) at $z \sim 1.2$ (panel a) while about half of the final total (disk + spheroid) stellar mass is only in place at $z \sim 0.8$ (panel b). About 20 per cent of this stellar mass is already in a spheroidal component (panel c). The mass of the spheroidal component grows in discrete steps as a consequence of our assumption that it grows during mergers and disk instability events, and approximately half of its final mass is already in a spheroidal component at $z \sim 2.5$. The cold gas mass content⁴, in contrast, varies much more gradually (panel d). Fig. 3 also shows that there is a very

⁴ Note that in our model, there is no cold gas in the spheroidal component. So all gas in panel (d) of Fig. 3 is associated to the disk.

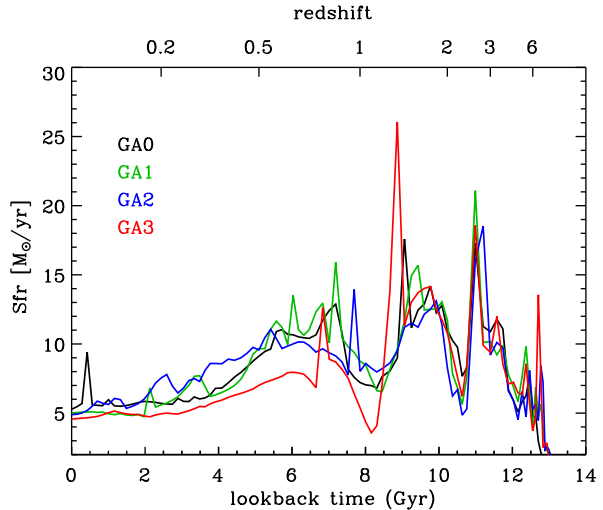


Figure 4. Star formation history of the model Milky Way galaxies from the four simulations used in this study (different colours).

weak increase of the stellar metallicity at late times: it only varies from ~ 0.75 solar to ~ 0.9 solar over the last 5 Gyr (panel e), while the gas-phase metallicity varies from ~ 1 solar to ~ 1.3 solar over the same interval of time. The more efficient enrichment of the gas component is due to the fact that in our model all metals produced by new stars are instantaneously returned to the cold phase, i.e. we are assuming a 100 per cent mixing efficiency of the metals with the cold gas already present at the time of star formation.

Interestingly, our model produces consistent evolutions for all four simulations used in our study, despite a very large increase in numerical resolution (see Table 1). This is particularly true for the stellar mass (panel a) and for the stellar metallicity (panel e). The amounts of gas (panel d) and metals in the gas phase (panel f) exhibit a much more noisy behaviour, but the overall evolution is still very similar. We note, however, that some panels (e.g. panels b, e, and f) do not show convergence of the results and this is driven by the lack of complete convergence in the N -body simulations (panel a shows a clear difference between GA3 and the lowest resolution simulations).

Fig. 4 shows the star formation history for the model Milky Way galaxies from the four simulations used in this study (colour coding as in Fig. 3). The star formation histories shown in Fig. 4 exhibit a quite bursty behaviour with several broad periods of enhanced star formation. In our models, these bursts are triggered by minor merger events. This intermittent behaviour is in qualitative agreement with the trend recovered by chromospheric age distributions of late-type dwarfs (Rocha-Pinto et al. 2000, and references therein). Fig. 4 also shows that the star formation rate declined slightly over the last ~ 4 Gyr and has a current value of $\sim 5 M_{\odot} \text{yr}^{-1}$. This trend is also in qualitative agreement with observational measurements (e.g. Hernandez, Valls-Gabaud & Gilmore 2000; Bertelli & Nasi 2001), but the level of star formation activity is significantly higher than the $\lesssim 1 M_{\odot} \text{yr}^{-1}$ estimated for the mean star formation rate in the Milky Way disc over the last few Gyrs (Just & Jahreiss 2007). Although the general behaviour is

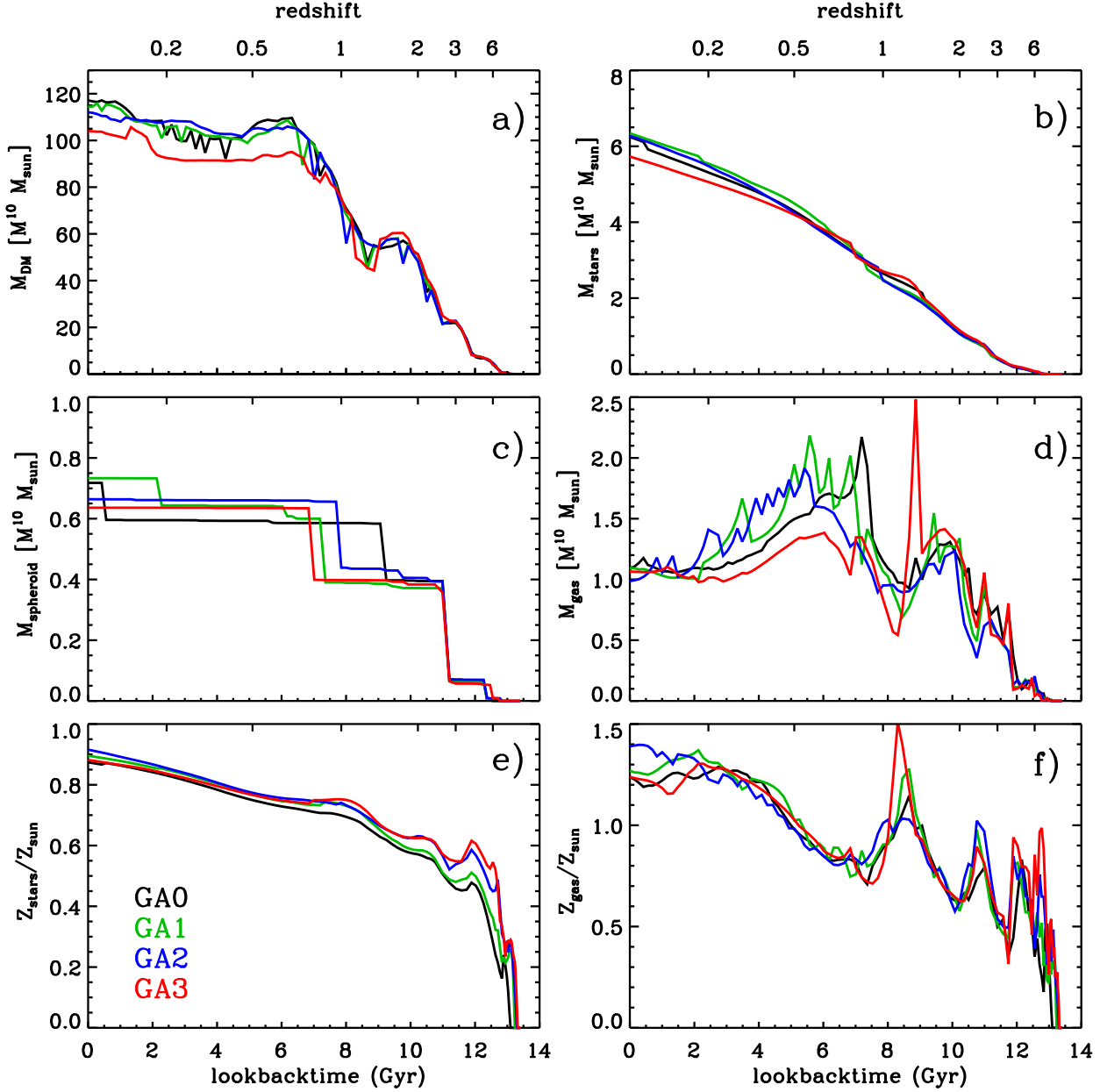


Figure 3. Evolution of the dark matter mass (panel a), total stellar mass (panel b), spheroid mass (panel c), cold gas mass (panel d), stellar metallicity (panel e), and gas metallicity (panel f) for the model Milky Way galaxies in the four simulations used in this study (different colours).

very similar for all four simulations used in this study, there is again no perfect convergence of the results, reflecting the behaviour of the available cold gas (panel d in Fig. 3).

For our default model and for the four simulations used in this study, the spheroid mass varies between $6.4 \times 10^9 M_{\odot}$ and $7.3 \times 10^9 M_{\odot}$ which is slightly lower than but still compatible with the observational estimate. As explained in the previous section, our model includes different channels for the formation of a spheroidal component: mergers (both minor and major) and disk instability. Fig. 3 (panel c) shows how the total mass in the spheroidal component grows as

a function of redshift. In Fig. 5, we show the cumulative fraction of the mass in the spheroidal component coming from minor mergers (solid coloured lines), and disk instability (dashed lines). Our model Milky Way galaxies do not experience any major merger during their life-times. In all four simulations used in our study, there are two episodes of disk instability, the first ~ 12 Gyr ago and the second ~ 1 Gyr later. Disk instability contributes in the range of 48 (GA1) to 58 (GA2) per cent of the final stellar mass in the spheroidal component. Minor mergers contribute to the remaining stellar mass in the spheroidal component, and

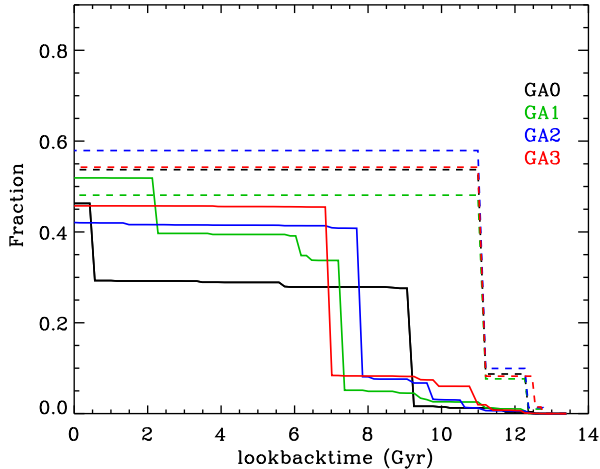


Figure 5. Cumulative fraction of the mass in the spheroidal component coming from minor mergers (solid lines) and from disk instability events (dashed lines), for the four simulations used in our study (different colours).

all occur at later times with respect to the disk instability episodes. As explained in Sec. 3, the stars formed during the bursts accompanying minor merger events, are added to the disk component. As a consequence, no spheroid star is formed *in situ* in our models.

As noted in Sec. 3, our model for disk instability is quite simplified and, given the uncertainties involved, the fraction of mass contributed by this channel should be considered as indicative. The results shown in Fig. 5 and Fig. 2 indicate that our default model would not produce a spheroid that is as massive as observed if the disk instability channel is switched off. On the other hand, it is now fairly well established that the Milky Way is a barred galaxy (Gerhard 2002, and references therein). Since global disk instabilities are commonly considered the main mechanism for the formation of a bar, the presence of a bar in the Milky Way is a direct indication that it has experienced episodes of disk instability during its life-time.

5 METALLICITY AND AGE DISTRIBUTIONS

As mentioned in Sec. 1, accurate measurements of ages, metallicity and kinematics have been collected for a large number of individual stars of our Galaxy, and a large amount of new observational measurements are expected in the near future. The available information is nicely summarised in Fig. 2 of Freeman & Bland-Hawthorn (2002).

The available data are indicative of a significant population of stars in the local disk with ages $\lesssim 8$ Gyr, and metallicity distribution (mostly from G/K dwarfs) that peaks at $[\text{Fe}/\text{H}] \sim -0.1$. From an analysis of the main sequence turn-off stars in the Hipparcos dataset, Binney, Dehnen & Bertelli (2000) obtained a best fit age for the oldest disk stars of $\gtrsim 11$ Gyr. The properties of the thick disk are relatively well known only within a few kpc from the Sun. In this region, typical thick disk stars have ages as old

as ~ 12 Gyr and intermediate metallicities ($[\text{Fe}/\text{H}] \sim -0.6$). For the Galactic bulge, deep HST and ISO colour-magnitude diagrams suggest a dominant old ($\gtrsim 10$ Gyr) population (Feltzing & Gilmore 2000; van Loon et al. 2003). The ISO data also suggest the presence of a small intermediate-age component which is traced by OH/IR stars (Sevenster 1999), but the interpretation is complicated by thin disk contamination. Bulge stars have a metallicity distribution that peaks at $[\text{Fe}/\text{H}] \sim -0.15$ dex, with a broad range and a tail to low abundances (McWilliam & Rich 1994, Zoccali et al. 2003, Fulbright, McWilliam & Rich 2006).

Fig. 6 shows the age and metallicity distribution of all stars (left panel) and of the stars in the spheroidal component (right panel) of our model Milky Way galaxy from the highest resolution simulation used in this study (results for lower resolution simulations are very similar). In each panel, black and white contours enclose the regions containing 99.6, and 60 per cent of the stars. On the right panel, solid contours refer to our fiducial model where stars can be transferred from the stellar disk component to the spheroid through disk instability. Dashed lines refer to a model with the same combination of parameters but with the disk instability channel switched off. Fig. 6 shows that the Galaxy contains stars of all ages - which reflects the prolonged star formation history shown in panel (g) of Fig. 3 - and covering a relatively limited range of metallicities centred around solar. The stars in the spheroidal component all have very old ages ($\gtrsim 11$ Gyr), their metallicity distribution peaks at sub-solar value and exhibit a pronounced tail of low metallicity stars. If spheroid growth through disk instability is switched off, the stars in the spheroidal component have a broader tail towards low and high abundances. The left panel of Fig. 6 shows a very shallow age-metallicity relation with a broader tail towards lower metallicities for older stars, in qualitative agreement with observational measurements (Nordström et al. 2004, see also Holmberg, Nordström & Andersen 2007). We caution the reader that the results shown in Fig. 6 represent a global average while observed samples represent a ‘local sample’. In addition, the model age-metallicity distributions are not convolved with typical observational errors which naturally tend to broaden the distributions.

The metallicity distributions (i.e. the projections along the y-axis of the maps shown in Fig. 6) of the stars in the disk and spheroid of our model galaxies are shown in Fig. 7. The left panels show the metallicity distribution of all stars (black histograms) and of the stars in the disk (blue histograms) compared to the observational measurements by Wyse & Gilmore (1995) (orange histogram in the top panel) and Nordström et al. (2004) (green histogram in the bottom panel). The sample of Wyse & Gilmore (1995) is a volume sample of long-lived thin disk G stars, while that of Nordström et al. (2004) contains a large ($\sim 14,000$) number of F/G dwarfs in the Solar neighbourhood (located at distances < 100 pc). In both these studies, metallicities were derived using a photometric calibration based on a relationship between $[\text{Fe}/\text{H}]$ and Strömgren colours (e.g. Schuster & Nissen 1989).

Fig. 7 thus shows that the metallicity distribution of disk stars in our model Milky Way peaks at approximately the same value as observed, but that it exhibits a deficiency of low metallicity stars. In comparing the model

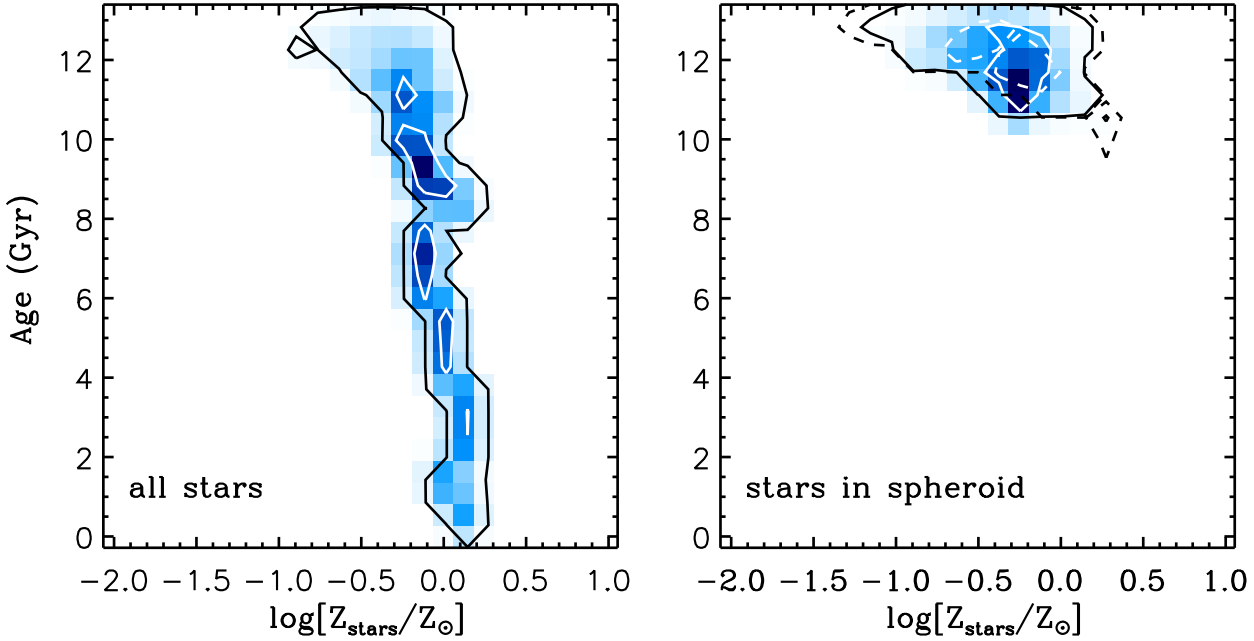


Figure 6. Age-metallicity distribution for all (left panel) and spheroid (right panel) stars of the model Milky Way from the highest resolution simulation used in this study (GA3). Black and white contour lines show regions that include 99.6 and 60 per cent of the stars used to build the corresponding map.

and observed metallicity distributions, however, two factors should be taken into account: (1) the observational metallicity measurements have some uncertainties (~ 0.2 dex) which tend to broaden the true underlying distribution; (2) the metallicity estimate used is an indicator of the *iron* abundance, which is mainly produced by supernovae Ia and therefore not well described by the instantaneous recycling approximation adopted in this study. In order to estimate the importance of this second caveat we have converted the measured $[\text{Fe}/\text{H}]$ into $[\text{O}/\text{H}]$ using a linear relation, which is obtained by fitting data for thin disk stars from Bensby, Feltzing & Lundström (2004). The result of this conversion is shown by the dashed orange histogram in the top panel of Fig. 7 for the original measurements by Wyse & Gilmore. The observed $[\text{O}/\text{H}]$ metallicity distribution is now much closer to the modelled $\log[\text{Z}/\text{Z}_\odot]$ distribution.

The right panels in Fig. 7 show the metallicity distribution of the spheroid stars in our fiducial model (red histogram) and in a model where the disk instability channel is switched off (dashed black histograms). In what follows, it may be useful to associate the stars originating in the disk instability to the bulge, and the rest of the spheroid stars to the stellar halo. Model results are compared to observational measurements by Zoccali et al. (2003) (orange histogram in the top panel) and recent results by Lecureur et al. (2007) and Zoccali et al. (2008) based on a sample of about 400 K-giants in two Galactic bulge windows, all observed with high dispersion spectra ($R > 20000$) with GIRAFFE on VLT (green histogram in the bottom panel). These panels show that the metallicity distribution of the model spheroid peaks at lower value than observed, and that it contains a

smaller fraction of high metallicity stars. Comparison between the solid red histogram and the black dashed histogram shows that the disk instability is responsible for the pronounced peak around $\text{Log}[\text{Z}/\text{Z}_\odot] \sim -0.25$ due to the transfer of a large fraction of disk stars into the spheroidal component, and which may be associated to the Galactic bulge component (Fig. 3 and Fig. 5 show that the mean metallicity of the stellar component is $\sim 0.6 Z_\odot$ at the time of the major episode of disk instability). The same caveat discussed above applies to the metallicity distribution of the spheroidal components. We note that a conversion from $[\text{Fe}/\text{H}]$ to $[\text{O}/\text{H}]$ of the observed metallicity scale would bring most of the observed bulge stars to $[\text{O}/\text{H}] \gtrsim -0.2$ suggesting that our model spheroid is significantly less metal rich than the observed Galactic bulge. However, we note that Fulbright et al. (2006) find a slightly more metal-poor distribution for the ‘Baade’s Window’, compared to the distribution found for the same field by Zoccali et al. (2008, plotted in the bottom right panel of Fig. 7). In addition, an outer bulge field (located at $b = -12$ deg) from Zoccali et al. (2008) peaks at lower metallicity compared to the metallicity distribution from the other two fields presented in the same study. This suggests that the uncertainties (as well as field to field variations) in the metallicity distribution of the bulge may alleviate the disagreement with our model results.

The metallicity distribution of the remainder spheroid stars (i.e. those originating in minor mergers) is relatively broad, and more metal-rich than observed for the Galactic stellar halo.

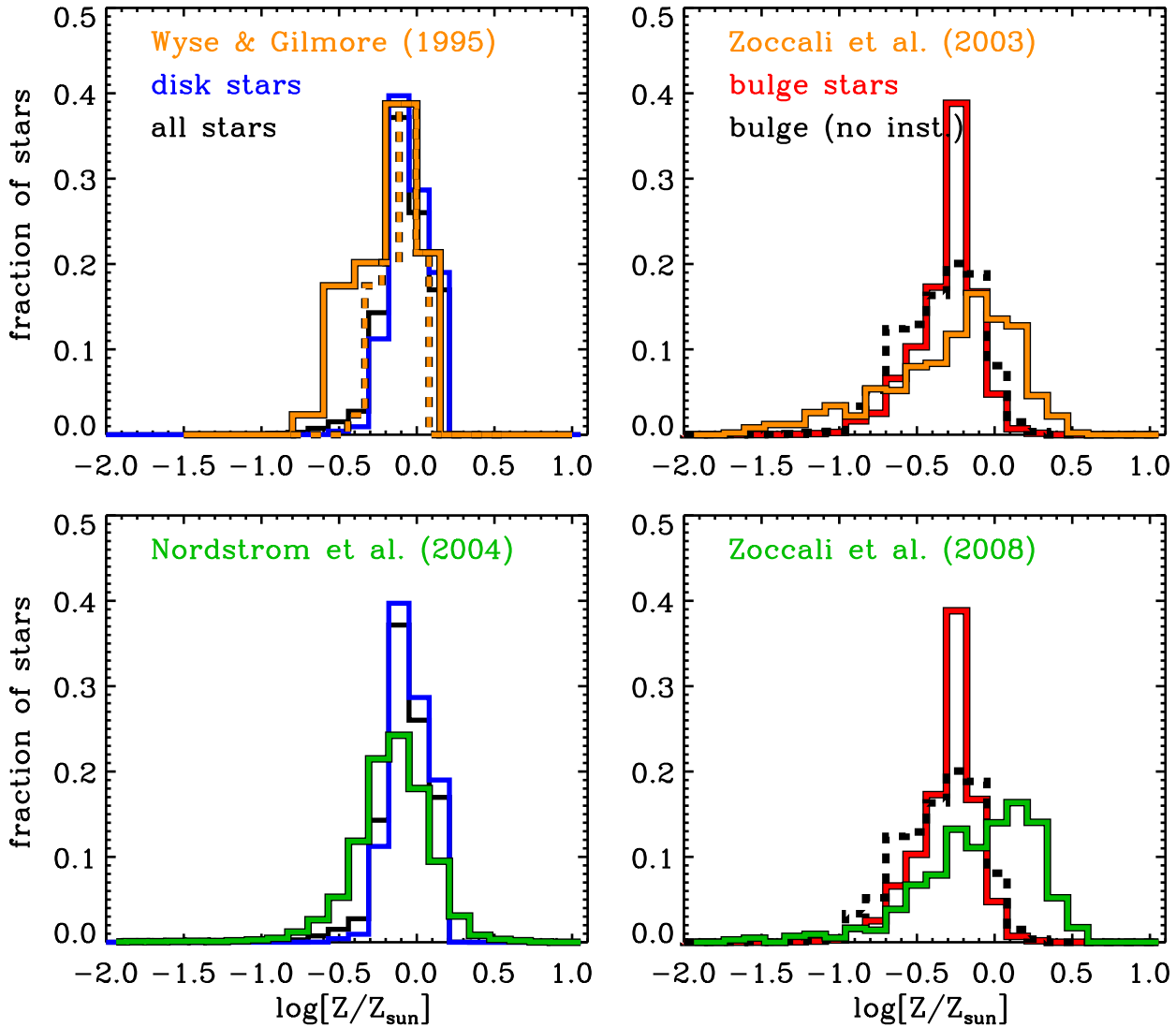


Figure 7. Metallicity distribution for stars in the disk (blue histograms in the left panels) and spheroid (red histograms in the right panels) of the model Milky Way from the highest resolution simulation in this study (GA3). The solid black histograms in the left panels show the metallicity distribution for all stars in the model galaxy, while the dashed black histograms in the right panels show the metallicity distribution of stars in the spheroidal component for our fiducial model if spheroid growth through disk instability is suppressed. Solid orange and green histograms show observational measurements by Wyse & Gilmore (1995, top left panel), Zoccali et al. (2003, top right panel), Nordström et al. (2004, bottom left panel), and Zoccali et al. (2008, bottom right panel). The dashed orange histogram in the top left panel has been obtained converting the $[\text{Fe}/\text{H}]$ scale of the original distribution by Wyse & Gilmore into an $[\text{O}/\text{H}]$ scale by using the observed $[\text{O}/\text{H}]-[\text{Fe}/\text{H}]$ relation for thin disk stars by Bensby, Feltz & Lundström (2004).

6 THE STELLAR HALO

As mentioned in Sec. 1, the stellar halo of our Galaxy has a mass that is less than about 1 per cent of the total stellar mass (i.e. about $10^9 M_{\odot}$). Most of its stars are very old (probably older than 12 Gyr) and metal-poor, with enhanced values of the elemental abundance ratio $[\alpha/\text{Fe}]$. The currently accepted scenario is that the stellar halo formed (at least in part) from stars stripped from satellite galaxies that were accreted by the Galaxy over its lifetime (the

Searle & Zinn scenario discussed in Sec. 1). In this section, we study the formation and structural properties of this galactic component, in the framework of the model discussed above.

Our working hypothesis is that the stellar halo built up from the cores of the satellite galaxies that merged with the Milky Way (or better its main progenitor - see below) over

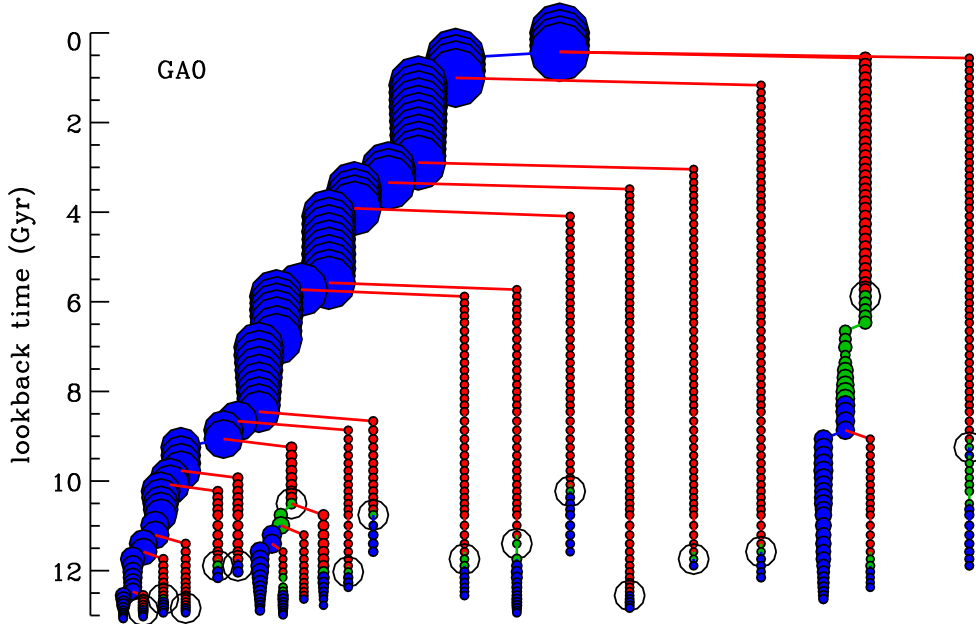


Figure 8. Full merger tree of our model Milky Way galaxy from the lowest resolution simulation used in this study (GA0). The area of the symbols scale with the number of particles of the associated halo, and their colour indicates different galaxy types: blue for galaxies sitting at the centre of the main halo (those on which cooling is allowed), green for satellites galaxies associated to distinct dark matter substructures, and red for ‘orphan’ galaxies (see text). The black circles mark the galaxies accreted onto the main branch of the model Galaxy, traced back until the last time they are central galaxies.

its lifetime.⁵ In order to identify the stars that end up in the stellar halo, we construct the full merger tree of our model Milky Way galaxy, and identify those galaxies that merge onto the ‘main branch’, i.e. the branch that is obtained by connecting the system to its most massive progenitor at each node of the tree (see Sec. 4.1 of De Lucia & Blaizot 2007). We then trace back each of these galaxies until they are for the last time central galaxies, and save the information (identification numbers and positions) of a fixed fraction of the most bound particles of their parent haloes at this time. We refer to these as ‘star particles’, and ‘tag’ them with the stellar metallicity of the galaxies residing at their centres.

The procedure outlined above is illustrated in Fig. 8 which shows the full merger tree of our model Milky-Way galaxy from the lowest resolution simulation used in our study (GA0). The Milky-Way galaxy is shown at the top of the plot, and all its progenitors and their histories are shown downward going back in time. In this figure, the area of the symbols scales with the number of particles in the associated halo, while different colours are used for different ‘types’ of galaxies. Central galaxies (the only ones on which cooling is allowed) are shown in blue. Green symbols indicate galaxies associated to a distinct dark matter substructure, and red symbols indicate ‘orphan’ galaxies, i.e. galaxies whose parent halo has been reduced below the resolution limit of the simulation. For visualisation purposes,

we have kept constant the mass of the dark matter substructure when a galaxy becomes orphan. The black circles in Fig. 8 mark the galaxies accreted onto the main branch of the model Galaxy (the leftmost branch in the figure), traced back until the last time they are central galaxies. In the following, we refer to this time as the *time of accretion*. Fig. 8 shows that the star particles that make up the stellar halo in GA0 are old: the majority of the satellites building up the stellar halo were ‘accreted’ at lookback times larger than ~ 9 Gyr (although about half of them ‘merge’ onto the main branch much later). Only one (relatively massive) satellite was accreted at lookback time ~ 8 Gyr, and it merges onto the main branch only at lookback time ~ 1 Gyr. For the simulations GA2 and GA3, all accretions occur at lookback times larger than ~ 11 Gyr. As we tag our star particles using the stellar populations of the central galaxies at the time of accretion, all stars in the stellar halo of these model galaxies have ages larger than 11 Gyr.

Fig. 8 illustrates that once dark matter haloes are accreted onto a larger system, they survive as distinct dark matter substructures for a relatively short time (e.g. De Lucia et al. 2004), but the galaxies residing at their centre merge onto the main progenitor of the Milky Way galaxy much later. As discussed in Sec. 3, our model galaxies are not affected by the tidal stripping and truncation that efficiently reduces the mass of the dark matter substructures (Ghigna et al. 2000; De Lucia et al. 2004; Gao et al. 2004). If this effect is important, the survival time-scales of orphan galaxies, as well as the stellar mass of survived satellites are

⁵ Note that some fraction of these galaxies may also contribute to the bulge component, particularly those with the highest density.

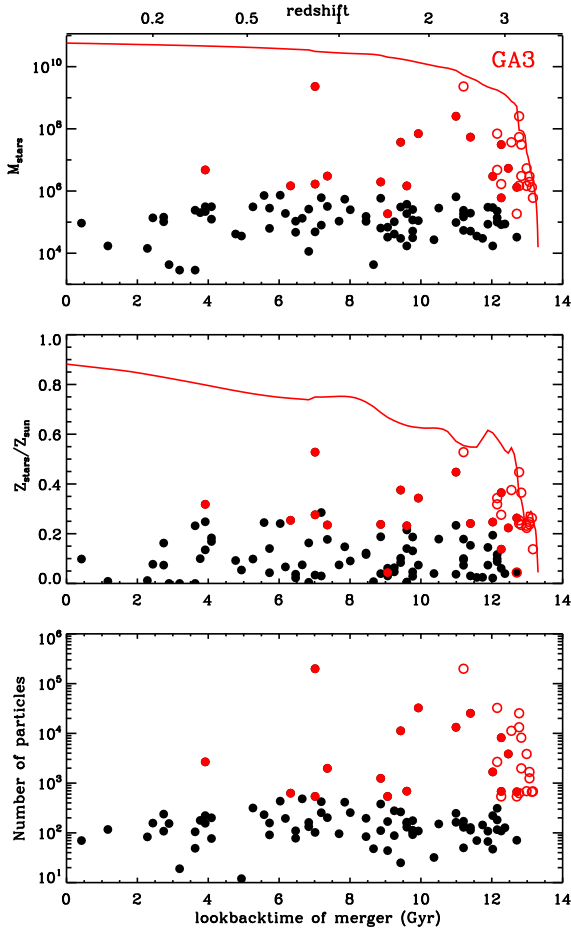


Figure 9. Stellar masses (top panel) and metallicities (middle panel) for all galaxies accreted onto the main branch for the simulation GA3, as a function of the lookback time of the galaxy’s merger. The solid red lines in the top and middle panels show the evolution of the stellar mass and metallicity in the main progenitor of the Milky Way. The bottom panel shows the number of particles associated to the dark matter halo at the time of accretion, again as a function of the merging time of the galaxy that is located at its centre. Red symbols indicate objects associated to substructures with more than 500 particles. Red open symbols correspond to red filled circles but are plotted as a function of the time of accretion.

likely to be overestimated. Work is underway to calibrate stellar tidal stripping using hydrodynamic simulations.

Fig. 9 shows the stellar masses (top panel) and metallicities (middle panel) of all galaxies accreted onto the main branch for the highest resolution simulation used in our study (GA3), as a function of the lookback time of the galaxy’s merger. Note that stellar masses and metallicities correspond to those at the time of accretion. The solid red lines in these panels show the evolution of the stellar mass and of the stellar metallicity in the main progenitor of the Milky Way galaxy (as in Fig. 3). The bottom panel of Fig. 9 shows the number of particles associated to the dark matter haloes before accretion, again as a function of the merging time of the galaxies that reside at their centre. Red sym-

bols indicate objects belonging to haloes with more than 500 bound particles before accretion. Note that for these objects we have indicated both the time of accretion (open symbols) and the merger time (solid symbols; given by the dynamical friction timescale as described above). The figure shows that most of the galaxies that merge onto the main branch have stellar masses and metallicities that are much smaller than the current mass of the main progenitor over most of the galaxy’s life-time. Most of the accreted galaxies lie in quite small haloes and only a handful of them are attached to relatively more massive systems. These are the galaxies that contribute most to the build-up of the stellar halo. The red symbols in the bottom panel of Fig. 9 show that most haloes with more than ~ 500 particles were all disrupted more than ~ 6 Gyr ago. These haloes contain the few galaxies with stellar mass larger than $10^6 M_{\odot}$ which merge onto the main branch over the galaxy’s life-time (top panel). The stellar metallicities are generally relatively low, with a median value of $\sim 0.3 Z_{\odot}$, with larger values associated to larger galaxies (see below). The results illustrated in Fig. 9 are in good agreement with those by Font et al. (2006) who find that one or a few more satellites in the range $10^8 - 10^{10} M_{\odot}$ can make up 50-80 per cent of the stellar halo and most of them are accreted early on ($t_{\text{accret}} > 9$ Gyr).

Fig. 10 shows the projected distribution of the star particles that end up in the stellar halo of the highest resolution simulation used in our study (GA3). For this figure, and for the results presented in the following, we use 10 per cent of the most bound particles of every accreted halo, but similar results are obtained if 5 per cent of the particles are selected. We obtain 4188 star particles for the simulation GA2, and 31716 star particles for the simulation GA3. The star particles in Fig. 10 are colour coded as a function of their metallicity, as indicated in the top-left panel, and their spatial distribution is shown at the same redshifts used for Fig. 1. The star particles that end up in the stellar halo extend over a projected region of $\sim 1 \text{ Mpc}^2$ comoving at redshift ~ 10 . At redshift ~ 1 , the star particles are already assembled in a single relatively elongated component which becomes progressively more spherical with decreasing redshift (see below). We note that the ‘stellar halo’ of the simulation GA3 is dominated by particles contributed by a single object that merged ~ 7 Gyr ago (and whose dark halo was accreted 11 Gyr ago) and with metallicity $0.53 Z_{\odot}$ (see Fig. 9). This single galaxy contributes 19921 star particles (i.e. about 60 per cent of all the star particles in the stellar halo).

The lower panels of Fig. 10 seems to suggest a slight concentration of the most metal-rich stars, but no clear correlation between metallicity and distance, with low metallicity and high metallicity stars distributed all at various distances. It is interesting that in some cases there is a clear difference between the mean metallicity of stars in a given satellite (pockets of stars of different colours) - which is the basis of the ‘chemical tagging’ argument discussed in Freeman & Bland-Hawthorn (2002). The resolution of the simulations used in this study is, however, too low to see any spatially coherent stellar streams in the halo at the present day.

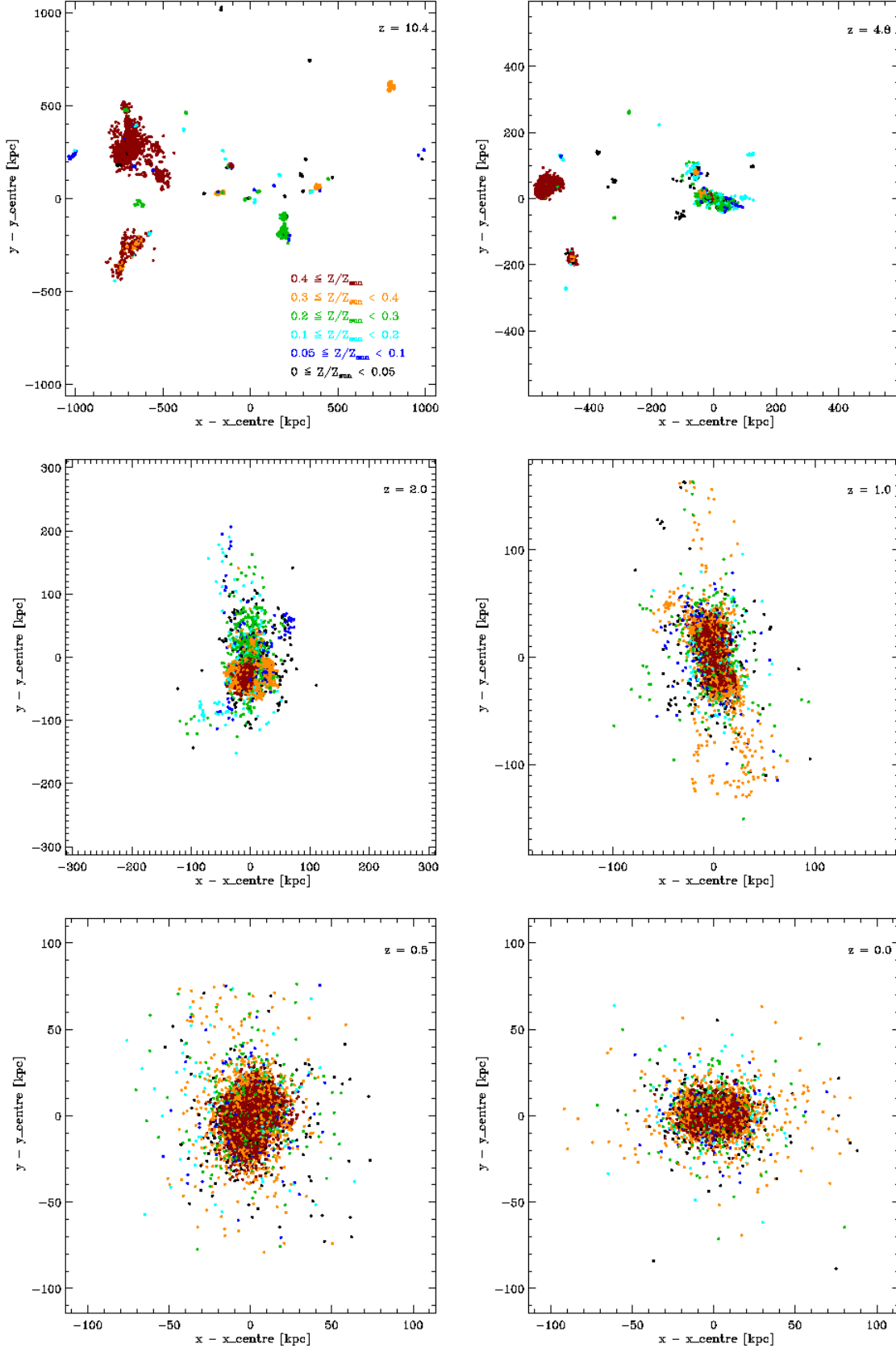


Figure 10. Projected distribution of the star particles that end up in the stellar halo of the highest resolution simulation used in our study (GA3), at the same redshifts as in Fig. 1, and colour-coded as a function of their metallicity as indicated in the top left panel. If we assume a $[\alpha/\text{Fe}] \sim +0.4$ dex, the highest metallicity bin could be translated into $-0.7 \lesssim [\text{Fe}/\text{H}]$, while the lowest to $[\text{Fe}/\text{H}] \lesssim -1.6$ (Salaris et al. 1993). As for Fig. 1, the box at $z = 0$ is centred on the most bound particle of the GA3 halo, while those at higher redshifts are centred on the most bound particle of the main progenitor at the corresponding redshift.

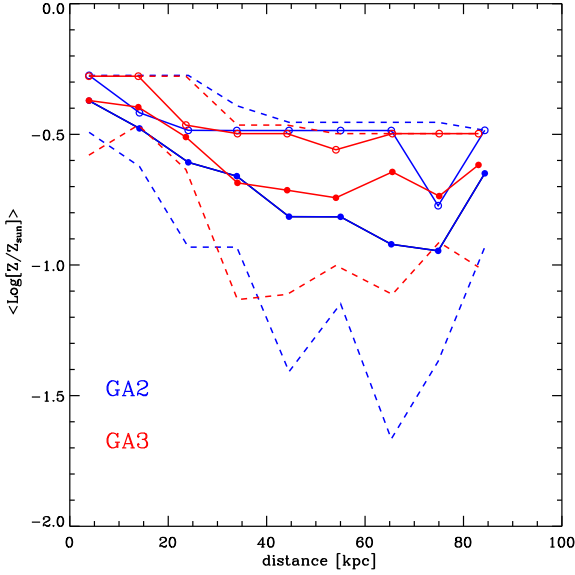


Figure 11. Mean (filled circles) and median (empty circles) metallicity of star particles as a function of the distance from the most bound particle in the Milky Way halo for the simulations GA2 (blue) and GA3 (red). Dashed lines correspond to the 15th and 85th percentiles of the distributions.

The absence of a clear metallicity gradient⁶ is illustrated more explicitly in Fig. 11 which shows the metallicity of the star particles as a function of the distance from the most bound particle in the Milky Way halo for the simulations GA2 (blue) and GA3 (red). Filled and empty circles connected by solid lines indicate the mean and the median of the distributions respectively. Dashed lines correspond to the 15th and 85th percentiles. In both simulations, the mean metallicity decreases from $\text{Log}[Z/Z_{\odot}] \sim -0.4$ at the centre to ~ -0.8 at a distance of ~ 40 kpc. The median and upper 85th percentile of both distributions are approximately flat around ~ -0.5 . The lower 15th percentile exhibits a certain decline with increasing distance from the centre, suggesting that the inner region is largely dominated by high-metallicity stars while the contribution from lower metallicity stars becomes more important moving to the outer regions. We recall, however, that both distributions are dominated in number by star particles associated to one or a few accreted galaxies with relatively high metallicity (hence the flat behaviour of the median and upper percentile): 58 per cent of the stellar halo particles in GA2 have metallicity ≥ -0.4 , and this fraction rises to 67 per cent for the simulation GA3. As discussed previously, the metallicity of our stellar halo is higher than what is known for the Galactic halo near the Sun. This could be reflecting that the metallicity of the accreted galaxies may be too high (see below).

From the observational viewpoint, it is interesting to ask where the most metal poor stars of the stellar halo are located. We address this question in Fig. 12 which shows the projected density profiles (solid black lines) of the star particles for the simulations GA2 (top panel) and GA3 (bot-

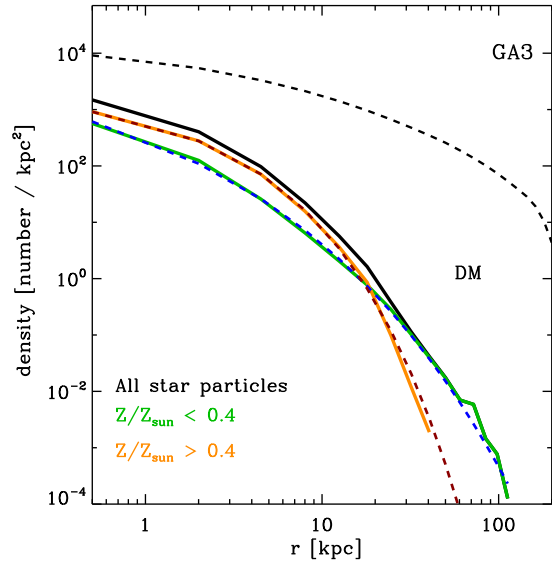
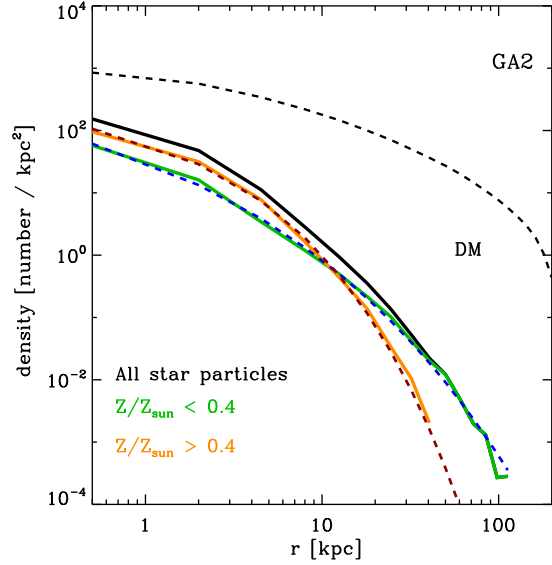


Figure 12. Projected density profile of the stellar halo (solid black lines) and of the dark matter halo (dashed black lines) for the simulations GA2 (top panel) and GA3 (bottom panel). The solid green and orange lines show the projected density profiles for star particles with metallicity smaller and larger than $0.4 Z_{\odot}$ respectively. The blue and red dashed lines show Sérsic fits to the profiles of star particles in the two metallicity bins.

tom panel) obtained by stacking the three projections on the xy , xz , and yz plane. The dashed black lines in Fig. 12 show the projected density profile of the dark matter halo⁷. In agreement with previous findings (Bullock & Johnston 2005), we find that the profile of the stellar halo is steeper and more centrally concentrated than the dark matter profile. The half-mass radius of the stellar halo in GA3 is located

⁶ We have verified that an age gradient is also absent.

⁷ We use only the particles in the ‘main halo’, i.e. the self-bound part of the friends-of-friends halo.

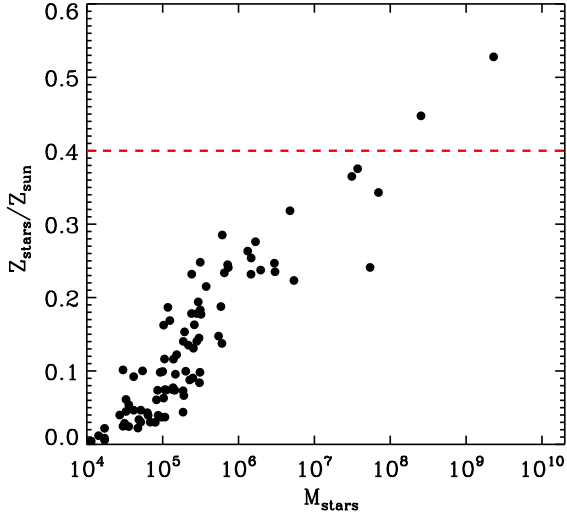


Figure 13. Stellar metallicity as a function of stellar mass for the galaxies contributing to the stellar halo in the simulation GA3.

at ~ 4.3 kpc, i.e. well within the Solar circle, as estimated for the Milky Way (Frenk & White 1982). The solid orange and green lines show the projected profiles of star particles with metallicity larger and smaller than $0.4 Z_{\odot}$ respectively. Fig. 12 shows that star particles with metallicity larger than $0.4 Z_{\odot}$ are more centrally concentrated than star particles of lower abundances. This implies that the probability of observing low-metallicity stars increases if one looks at larger distances from the Galactic centre ($\gtrsim 10$ – 20 kpc) where the contribution from the inner more metal-rich star particles is less dominant.

Interestingly, our results appear to be in qualitative agreement with the measurements by Carollo et al. (2007). These authors have analysed a large sample of over 20,000 stellar spectra from SDSS, and demonstrated that the stellar halo of the Milky Way can be considered as the superposition of two components which are spatially, kinematically, and chemically distinct. One component, which they call ‘inner halo’, dominates the population of stars found at distances up to 10–15 kpc from the Galactic centre and peaks at higher metallicity than the ‘outer halo’, which dominates in regions beyond 15–20 kpc.

In order to understand this ‘duality’ we turn to our simulations. From the middle panel of Fig. 9 we see that stellar metallicity does not correlate with the time of the merger of the galaxies that contribute to the stellar halo. Rather, the ‘duality’ of our model stellar halo originates from a correlation between the stellar metallicity and the mass in stars of the accreted galaxies, as shown in Fig. 13. Since the most massive galaxies can decay through dynamical friction to the inner regions of the host halo, this is where higher metallicity stars will be found preferentially. Note that the mass-metallicity relation in our simulations appears to be offset from that observed in the sense that the accreted galaxies are too metal-rich, explaining why our stellar halo also has too high a metallicity. This might be due to a too efficient mixing of metals with the intergalactic medium (we recall that we are using a 100 per cent mixing efficiency), and/or

Table 3. Results of the Sérsic fit (see text) to the projected profiles of star particles with metallicity larger and smaller than $0.4 Z_{\odot}$ (orange and green lines in Fig. 12).

$Z < 0.4 Z_{\odot}$	R_{eff} [kpc]	n
GA2	4.1	3.3
GA3	4.9	3.0
$Z \geq 0.4 Z_{\odot}$	R_{eff} [kpc]	n
GA2	4.7	1.9
GA3	4.4	1.6

to inefficient feedback in the building blocks of the stellar halo. We will analyse this in further detail in a future paper where we will study the satellite population of our model Milky Way.

A large fraction of galaxies accreted onto the main branch contribute to the star particles in the inner halo⁸, i.e. $r < 10$ kpc, but only a few systems contribute significantly to the population of star particles in this region. For both simulations, about 65 per cent of the star particles in the inner region comes from one single system that merged onto the main branch ~ 8 Gyr ago for the simulation GA2, and ~ 7 Gyr ago for the simulation GA3. Another ~ 20 per cent of the star particles in the inner 10 kpc are contributed in approximately equal fractions from other three galaxies that merged between ~ 8 and ~ 10.5 Gyr ago for the simulation GA2, and a bit earlier (between ~ 10 and ~ 11.5 Gyr ago) for the simulation GA3.

The blue and red dashed lines in Fig. 12 show Sérsic fits to the star particles with metallicity larger and smaller than $0.4 Z_{\odot}$ respectively (corresponding to the orange and green lines). The fitted function is given by:

$$\Sigma(R) = \Sigma_{\text{eff}} \exp \left[-b_n \left[\left(R/R_{\text{eff}} \right)^{1/n} - 1 \right] \right]$$

where R_{eff} is the radius containing half the light and Σ_{eff} is the surface brightness at that radius. The results of the fit are given in Table 3. For both simulations, the profile of star particles with metallicity lower than $0.4 Z_{\odot}$ is well fit by a Sérsic profile with index $n \sim 3$ and half-light radius ~ 4 kpc. For the star particles with larger metallicity the characteristic radius is comparable, and the Sérsic index is smaller (the distribution falls off more steeply). The logarithmic slope of the corresponding density profile at R_{eff} is $\gamma \sim -3.3$ for the metal-rich component and $\gamma \sim -3.1$ for the metal-poor stars, in very good agreement with those measured for the stellar halo of the Milky Way at a similar galactocentric distance.

In order to characterise the three-dimensional shape of the stellar halo, we have assumed that its isodensity surfaces can be approximated by triaxial ellipsoids of the form:

$$\frac{X_1^2}{a^2} + \frac{X_2^2}{b^2} + \frac{X_3^2}{c^2} = 1 \quad \text{with } a \geq b \geq c$$

where a , b , and c are the lengths of the three axes and X_{α} (with $\alpha = 1, 2, 3$) is the coordinate with respect to the α

⁸ 70 and 95 per cent of the accreted galaxies contribute at least one particle to this region of the stellar halo for the simulations GA2 and GA3 respectively.

Table 4. Axial ratios for the stellar halo and for the dark matter halo of the Milky Way galaxy for the simulations GA2 and GA3 used in this study.

stellar halo	c/a	c/b
GA2	0.51	0.74
GA3	0.45	0.89
dark matter halo	c/a	c/b
GA2	0.70	0.80
GA3	0.72	0.85

axis and relative to the position of the most bound particle of the Milky Way halo. The directions and lengths of the major axes can then be computed by finding the eigenvectors and eigenvalues of the matrix $M_{\alpha\beta}$:

$$M_{\alpha\beta} = \sum_i X_{\alpha}^i X_{\beta}^i$$

where $\alpha, \beta = 1, 2, 3$. In Table 4, we list the resulting axial ratios c/a and c/b for the stellar halo and for the dark matter halo, for the simulations GA2 and GA3. The principal axes of the stellar halo and of the dark matter halo are plotted as thin and thick solid lines in Fig. 14. The top panel corresponds to the simulation GA2, while the bottom panel is for the simulations GA3. In both panels, orange and green points are star particles with metallicity larger and smaller than $0.4 Z_{\odot}$.

The value of the short-to-long (c/a) axis ratio measured for the dark matter halo is in good agreement with previous numerical studies in a Λ CDM cosmology by Bullock (2002) who finds typical axis ratios to be $c/a \sim 0.6 - 0.8$ for Milky Way size haloes. The stellar halo has a short-to-long axis ratio $\sim 0.45 - 0.5$, slightly lower than observational measurements (Chiba & Beers 2000; Bell et al. 2007, and references therein). Interestingly, for both simulations the minor axis of the stellar halo is quite well aligned with the the minor axis of the dark matter halo: the angle between these two axes is only ~ 10 deg for the simulation GA2 and ~ 30 deg for the simulation GA3. For the highest resolution simulation (GA3), also the major and intermediate axes of the stellar halo are well aligned with the corresponding axes of the dark matter halo (the angular distance is ~ 9 and ~ 30 deg for the other two axes). For the simulation GA2, the angular distance between the major and intermediate axes of the stellar halo and the corresponding axes of the main halo is ~ 75 deg.

7 DISCUSSION AND CONCLUSIONS

During the last decade, a number of observational tests of the standard cosmological model have ushered in a new era of ‘precision cosmology’. While the basic theoretical paradigm for structure formation is now well established, our understanding of the physical processes governing galaxy formation and evolution is far from complete. Modern advances in ground- and space-based observational capabilities have enabled us to study the resolved stellar populations of Local Group galaxies (and beyond) in unprecedented detail. For our own Galaxy and for a number of the brightest mem-

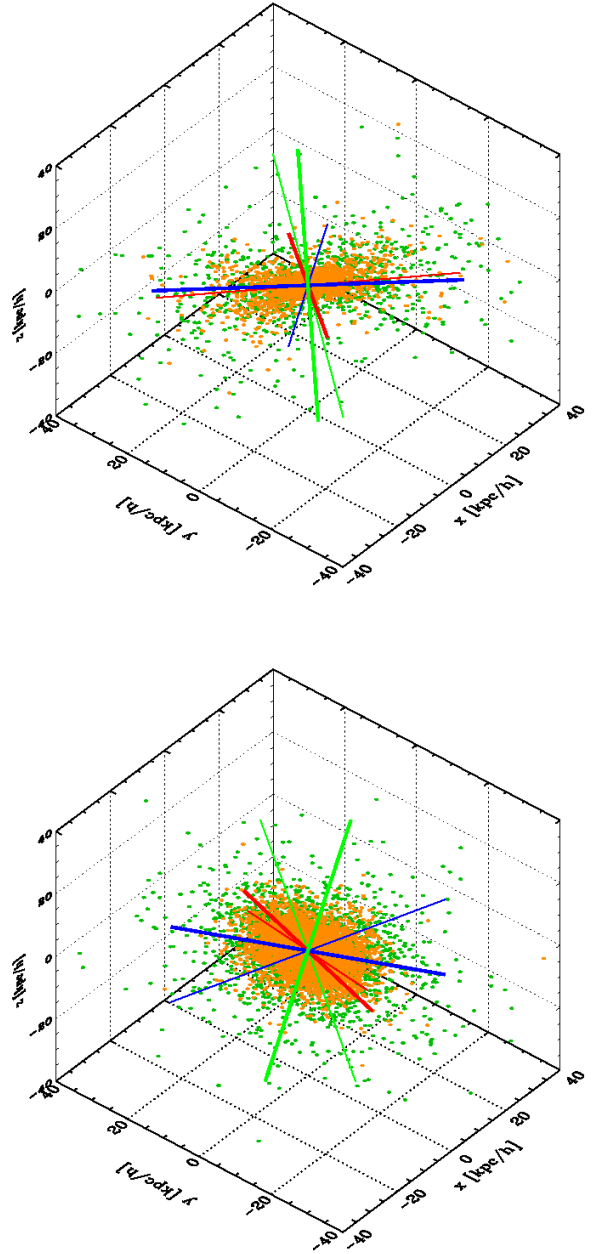


Figure 14. Three-dimensional distribution of the star particles from the simulations GA2 (top panel) and GA3 (bottom panel). Green symbols refer to particles with $Z/Z_{\odot} < 0.4$, while orange symbols refer to star particles with $Z/Z_{\odot} \geq 0.4$. Red, blue and green lines represent the principal axes of the stellar halo (thin lines) and of the dark matter halo (thick lines). Red is used for the long axis, blue for the intermediate, and green for the short axis.

bers of the Local Group, a wealth of observational data is now available about the ages and chemical abundances of their stars. Much more data will become available over the next decade, providing important tests for current models of galaxy formation and evolution.

In this paper, we have discussed the formation of the Milky Way and of its stellar halo in the context of a hybrid

cosmological approach that combines high-resolution simulations of a ‘Milky-Way’ halo with semi-analytic methods.

Our approach is similar to that adopted by Bullock & Johnston (2005), but the two methods differ in a number of details. Bullock & Johnston have used mass accretion histories of Milky Way-size galaxies using the extended Press-Schechter formalism. For each accretion event in the analytic merger trees, they have run N -body simulations following the dynamical evolution of the accreted dark matter satellite in an analytic parent galaxy+host halo potential. The stellar distribution and properties of each satellite are constructed using a variable mass-to-light ratio to each dark matter particle (Font et al. 2006), and the chemical evolution of the satellites is modelled taking into account the enrichment from both Type II and Type Ia supernovae (Robertson et al. 2005). In our work, we have used a set of increasing resolution N -body simulations of a Milky Way-like halo, combined with a semi-analytic method that allows us to model the stellar distribution of the galaxies self-consistently during the N -body simulation. While our approach is based on a fully numerical simulation, the numerical resolution for each accreted satellite is lower than that achieved by Bullock & Johnston. In addition, our chemical evolution model assumes an instantaneous recycling approximation which is appropriate for elements produced by Type II supernovae, but wrong for the iron-peak elements which are mainly produced by Type Ia supernovae.

The galaxy formation model employed in this work has been studied in a number of previous papers, and it has been shown to successfully reproduce a number of observational results for the global galaxy population in the local Universe and at higher redshifts. The physical properties of our model Milky-Way galaxies are in quite nice agreement with the observational results, and the predicted evolutions are very similar, over the entire numerical range covered by the simulations used in our work (from $\sim 2 \times 10^8$ to $\sim 3 \times 10^5 M_\odot$ dark matter particle mass). This is the first time to our knowledge that model convergence has been shown on a galaxy-by-galaxy basis⁹.

Our model Milky Way galaxy is a relatively young system (50 per cent of the stars are assembled in a single object only at redshift ~ 0.8) with a very old spheroidal component (50 per cent of the stars in the spheroid are in place at redshift ~ 3), which is formed through a series of minor mergers and a few episodes of disk instability occurring early on during the galaxy’s lifetime. All stars in the spheroidal component are old ($\gtrsim 11$ Gyr) while the stars in the disk have a much larger spread in age, reflecting a prolonged star formation activity which is in qualitative agreement with observational determinations. A detailed comparison between model and observed metallicity distributions is complicated by the use of the instantaneous recycling approximation, which does not allow direct comparison with the observed iron distribution. Using the observed relation between oxygen and iron abundances, we obtain a metallicity distribution which is similar to the observed one for the disk component, but a spheroidal component which is less

enriched than the observed Galactic bulge (although small changes in the parameters of the semi-analytic models are able to remove this discrepancy without significantly affecting the remaining properties of the simulated Galaxy, see e.g Fig. 2).

Assuming that the stellar halo builds up from the cores of the satellite galaxies that merged with the Milky Way over its life-time, we are able to study the physical and structural properties of this Galactic component. Our model stellar halo is made up of very old stars (the majority of the stars formed earlier than 10 Gyr ago) with low metallicity ($\lesssim 0.5 Z_\odot$), although relatively high in comparison to the Galactic halo near the Sun. A few relatively massive ($10^8 - 10^{10} M_\odot$) satellites accreted early (> 9 Gyr) contribute the largest fraction of the star particles that end up in the stellar halo, in agreement with previous results by Font et al. (2006). There is no evidence of a metallicity gradient for halo stars, but we find evidence for a stronger concentration of higher metallicity stars. This implies that the probability of observing low-metallicity halo stars increases with distance from the Galactic centre ($\gtrsim 20$ kpc). The ‘duality’ we find for our model stellar halo does not originate from a correlation between metallicity and accretion time, rather from the fact that the main contributors to the stellar halo (satellites with larger mass) have preferentially higher metallicity than lower mass systems. We find that the three-dimensional distribution of halo stars is well described by a triaxial ellipsoid with short-to-long axis $\sim 0.5 - 0.6$, in agreement with observational measurements, and whose axes are well aligned to those of the parent dark matter halo.

A more accurate treatment of chemical enrichment will allow us to carry out a more detailed comparison with observed chemical compositions, and to establish similarities and differences between present-day satellites and the Galactic building blocks. The numerical resolution of the simulations used in this work, however, is too low for studies of spatially and kinematically coherent stellar streams in the present day stellar halo. Higher resolution simulations are therefore needed for these studies. These are all much needed steps to interpret the outcome of large surveys such as SEGUE, RAVE and ultimately Gaia, with the goal of unrevealing the evolutionary history of our Galaxy.

ACKNOWLEDGEMENTS

We are indebted to Felix Stoehr for making his GA series available, and to Volker Springel for making available the substructure finder and merger tree construction software that was originally developed for the Millennium Simulation project (<http://www.mpa-garching.mpg.de/galform/virgo/millennium/>). We thank K. Dolag for help in adapting the software to the simulation outputs, M. Zoccali for providing observational measurements prior to publication, and Y.S. Li for useful discussions. We thank Simon White for encouragement in completing this project. GDL acknowledges the hospitality of the Kapteyn Astronomical Institute of Groningen, where this project was initiated. AH gratefully acknowledges financial support from the Netherlands Organisation for Scientific Research (NWO) and from the Netherlands

⁹ Springel et al. (2001) discussed the convergence of model results in statistical sense using a set of four high-resolution N -body simulations of galaxy clusters.

Research School for Astronomy (NOVA). GDL thanks D. Gadotti for useful discussions about bar formation and evolution, U. Maio for refreshing discussions about eigenvalues and eigenvectors, and A. Moretti for useful comments on a preliminary version of this paper, as well as for continuous support in the last year.

This paper has been typeset from a $\text{\TeX}/\text{\LaTeX}$ file prepared by the author.

REFERENCES

- Abadi M. G., Navarro J. F., Steinmetz M., 2006, *MNRAS*, 365, 747
- Battaglia G., Helmi A., Morrison H., Harding P., Olszewski E. W., Mateo M., Freeman K. C., Norris J., Shtetman S. A., 2005, *MNRAS*, 364, 433
- Baugh C. M., 2006, *Reports of Progress in Physics*, 69, 3101
- Beers T. C., Allende Prieto C., Wilhelm R., Yanny B., Newberg H., 2004, *Publications of the Astronomical Society of Australia*, 21, 207
- Bell E. F., Zucker D. B., Belokurov V., Sharma S., Johnston K. V., Bullock J. S., Hogg D. W., Jahnke K., de Jong J. T. A., Beers T. C., Evans N. W., Grebel E. K., Ivezić Z., Koposov S. E., Rix H.-W., Schneider D. P., Steinmetz M., Zolotov A., 2007, *ArXiv e-prints*, 706
- Bensby T., Feltzing S., Lundström I., 2004, *A&A*, 415, 155
- Benson A. J., Cole S., Frenk C. S., Baugh C. M., Lacey C. G., 2000, *MNRAS*, 311, 793
- Berentzen I., Shlosman I., Martinez-Valpuesta I., Heller C. H., 2007, *ApJ*, 666, 189
- Bertelli G., Nasi E., 2001, *AJ*, 121, 1013
- Binney J., Dehnen W., Bertelli G., 2000, *MNRAS*, 318, 658
- Bissantz N., Debattista V. P., Gerhard O., 2004, *ApJ*, 601, L155
- Blitz L., 1997, in Latter W. B., Radford S. J. E., Jewell P. R., Mangum J. G., Bally J., eds, *IAU Symposium Vol. 170 of IAU Symposium, CO in the Milky Way*. p. 11
- Boylan-Kolchin M., Ma C.-P., Quataert E., 2008, *MNRAS*, 383, 93
- Bullock J. S., 2002, in Natarajan P., ed., *Proceedings of the Yale Cosmology Workshop "The Shapes of Galaxies and Their Dark Matter Halos"* Shapes of dark matter halos. p. 109
- Bullock J. S., Johnston K. V., 2005, *ApJ*, 635, 931
- Carney B. W., Latham D. W., Laird J. B., 1989, *AJ*, 97, 423
- Carollo D., Beers T. C., Lee Y. S., Chiba M., Norris J. E., Wilhelm R., Sivarani T., Marsteller B., Munn J. A., Bailer-Jones C. A. L., Fiorentin P. R., York D. G., 2007, *Nature*, 450, 1020
- Chiba M., Beers T. C., 2000, *AJ*, 119, 2843
- Cole S., 1991, *ApJ*, 367, 45
- Croton D. J., Springel V., White S. D. M., De Lucia G., Frenk C. S., Gao L., Jenkins A., Kauffmann G., Navarro J. F., Yoshida N., 2006, *MNRAS*, 365, 11
- Curir A., Mazzei P., Murante G., 2007, *A&A*, 467, 509
- De Lucia G., Blaizot J., 2007, *MNRAS*, 375, 2
- De Lucia G., Kauffmann G., Springel V., White S. D. M., Lanzoni B., Stoehr F., Tormen G., Yoshida N., 2004, *MNRAS*, 348, 333
- De Lucia G., Kauffmann G., White S. D. M., 2004, *MNRAS*, 349, 1101
- De Lucia G., Springel V., White S. D. M., Croton D., Kauffmann G., 2006, *MNRAS*, 366, 499
- Diemand J., Madau P., Moore B., 2005, *MNRAS*, 364, 367
- Dwek E., Arendt R. G., Hauser M. G., Kelsall T., Lisse C. M., Moseley S. H., Silverberg R. F., Sodroski T. J., Weiland J. L., 1995, *ApJ*, 445, 716
- Efstathiou G., Lake G., Negroponte J., 1982, *MNRAS*, 199, 1069
- Eggen O. J., Lynden-Bell D., Sandage A. R., 1962, *ApJ*, 136, 748
- Feltzing S., Gilmore G., 2000, *A&A*, 355, 949
- Font A. S., Johnston K. V., Bullock J. S., Robertson B. E., 2006, *ApJ*, 638, 585
- Freeman K., Bland-Hawthorn J., 2002, *ARA&A*, 40, 487
- Frenk C. S., White S. D. M., 1982, *MNRAS*, 198, 173
- Fulbright J. P., McWilliam A., Rich R. M., 2006, *ApJ*, 636, 821
- Gao L., White S. D. M., Jenkins A., Stoehr F., Springel V., 2004, *MNRAS*, 355, 819
- Gerhard O., 2002, in Da Costa G. S., Jerjen H., eds, *The Dynamics, Structure & History of Galaxies: A Workshop in Honour of Professor Ken Freeman Vol. 273 of Astronomical Society of the Pacific Conference Series, The Galactic Bar*. p. 73
- Ghigna S., Moore B., Governato F., Lake G., Quinn T., Stadel J., 2000, *ApJ*, 544, 616
- Gilmore G., Reid N., 1983, *MNRAS*, 202, 1025
- Gilmore G., Wyse R. F. G., Norris J. E., 2002, *ApJ*, 574, L39
- Hatton S., Devriendt J. E. G., Ninin S., Bouchet F. R., Guiderdoni B., Vibert D., 2003, *MNRAS*, 343, 75
- Helmi A., 2008, *A&A Rev.*, 15, 145
- Helmi A., Irwin M. J., Tolstoy E., Battaglia G., Hill V., Jablonka P., Venn K., Shetrone M., Letarte B., Arimoto N., Abel T., Francois P., Kaufer A., Primas F., Sadakane K., Szeifert T., 2006, *ApJ*, 651, L121
- Helmi A., Navarro J. F., Nordström B., Holmberg J., Abadi M. G., Steinmetz M., 2006, *MNRAS*, 365, 1309
- Helmi A., White S. D. M., de Zeeuw P. T., Zhao H., 1999, *Nature*, 402, 53
- Helmi A., White S. D. M., Springel V., 2003, *MNRAS*, 339, 834
- Hernandez X., Valls-Gabaud D., Gilmore G., 2000, *MNRAS*, 316, 605
- Holmberg J., Nordström B., Andersen J., 2007, *A&A*, 475, 519
- Ibata R. A., Gilmore G., Irwin M. J., 1994, *Nature*, 370, 194
- Jiang C. Y., Jing Y. P., Faltenbacher A., Lin W. P., Li C., 2008, *ApJ*, 675, 1095
- Just A., Jahreiss H., 2007, *ArXiv e-prints*, 706
- Kauffmann G., Colberg J. M., Diaferio A., White S. D. M., 1999, *MNRAS*, 303, 188
- Kauffmann G., White S. D. M., Guiderdoni B., 1993, *MNRAS*, 264, 201
- Kazantzidis S., Mayer L., Mastropietro C., Diemand J., Stadel J., Moore B., 2004, *ApJ*, 608, 663

- Kennicutt Jr. R. C., 1989, *ApJ*, 344, 685
- Kitzbichler M. G., White S. D. M., 2007, *MNRAS*, 376, 2
- Kitzbichler M. G., White S. D. M., 2008, *ArXiv e-prints*, 804
- Kuijken K., Rich R. M., 2002, *AJ*, 124, 2054
- Lecureur A., Hill V., Zoccali M., Barbuy B., Gómez A., Minniti D., Ortolani S., Renzini A., 2007, *A&A*, 465, 799
- Majewski S. R., Munn J. A., Hawley S. L., 1996, *ApJ*, 459, L73
- Martin N. F., Ibata R. A., Bellazzini M., Irwin M. J., Lewis G. F., Dehnen W., 2004, *MNRAS*, 348, 12
- Martinez-Valpuesta I., Shlosman I., Heller C., 2006, *ApJ*, 637, 214
- McWilliam A., Rich R. M., 1994, *ApJS*, 91, 749
- Mo H. J., Mao S., White S. D. M., 1998, *MNRAS*, 295, 319
- Nordström B., Mayor M., Andersen J., Holmberg J., Pont F., Jørgensen B. R., Olsen E. H., Udry S., Mowlavi N., 2004, *A&A*, 418, 989
- Peñarrubia J., Benson A. J., 2005, *MNRAS*, 364, 977
- Perryman M. A. C., de Boer K. S., Gilmore G., Høg E., Lattanzi M. G., Lindegren L., Luri X., Mignard F., Pace O., de Zeeuw P. T., 2001, *A&A*, 369, 339
- Robertson B., Bullock J. S., Font A. S., Johnston K. V., Hernquist L., 2005, *ApJ*, 632, 872
- Rocha-Pinto H. J., Scalo J., Maciel W. J., Flynn C., 2000, *A&A*, 358, 869
- Salaris M., Chieffi A., Straniero O., 1993, *ApJ*, 414, 580
- Salvadori S., Ferrara A., Schneider R., 2008, *astro-ph/0802.0462*, 802
- Schödel R., Ott T., Genzel R., Hofmann R., Lehnert M., Eckart A., Mouawad N., Alexander T., et al. 2002, *Nature*, 419, 694
- Schuster W. J., Nissen P. E., 1989, *A&A*, 221, 65
- Searle L., Zinn R., 1978, *ApJ*, 225, 357
- Sellwood J. A., 1989, *MNRAS*, 238, 115
- Sellwood J. A., Moore E. M., 1999, *ApJ*, 510, 125
- Sevenster M. N., 1999, *MNRAS*, 310, 629
- Shetrone M. D., Côté P., Sargent W. L. W., 2001, *ApJ*, 548, 592
- Simon J. D., Bolatto A. D., Leroy A., Blitz L., 2003, *ApJ*, 596, 957
- Smith M. C., Ruchti G. R., Helmi A., Wyse R. F. G., Fulbright J. P., Freeman K. C., Navarro J. F., Seabroke G. M., et al. 2007, *MNRAS*, 379, 755
- Springel V., White S. D. M., Jenkins A., Frenk C. S., Yoshida N., Gao L., Navarro J., Thacker R., Croton D., Helly J., Peacock J. A., Cole S., Thomas P., Couchman H., Evrard A., Colberg J., Pearce F., 2005, *Nature*, 435, 629
- Springel V., White S. D. M., Tormen G., Kauffmann G., 2001, *MNRAS*, 328, 726
- Springel V., Yoshida N., White S. D. M., 2001, *New Astronomy*, 6, 79
- Steinmetz M., Zwitter T., Siebert A., Watson F. G., Freeman K. C., Munari U., Campbell R., Williams M., et al. 2006, *AJ*, 132, 1645
- Stewart K. R., Bullock J. S., Wechsler R. H., Maller A. H., Zentner A. R., 2007, *ArXiv e-prints*, 711
- Stoehr F., 2006, *MNRAS*, 365, 147
- Stoehr F., White S. D. M., Springel V., Tormen G., Yoshida N., 2003, *MNRAS*, 345, 1313
- Stoehr F., White S. D. M., Tormen G., Springel V., 2002, *MNRAS*, 335, L84
- Strigari L. E., Bullock J. S., Kaplinghat M., Diemand J., Kuhlen M., Madau P., 2007, *ApJ*, 669, 676
- Tolstoy E., Venn K. A., Shetrone M., Primas F., Hill V., Kaufer A., Szeifert T., 2003, *AJ*, 125, 707
- Tormen G., Bouchet F. R., White S. D. M., 1997, *MNRAS*, 286, 865
- van Loon J. T., Gilmore G. F., Omont A., Blommaert J. A. D. L., Glass I. S., Messineo M., Schuller F., Schultheis M., Yamamura I., Zhao H. S., 2003, *MNRAS*, 338, 857
- Venn K. A., Irwin M., Shetrone M. D., Tout C. A., Hill V., Tolstoy E., 2004, *AJ*, 128, 1177
- Wang J., De Lucia G., Kitzbichler M. G., White S. D. M., 2007, *astro-ph/0706.2551*
- Wang L., Li C., Kauffmann G., De Lucia G., 2006, *MNRAS*, 371, 537
- White S. D. M., Frenk C. S., 1991, *ApJ*, 379, 52
- White S. D. M., Rees M. J., 1978, *MNRAS*, 183, 341
- Wyse R. F. G., Gilmore G., 1995, *AJ*, 110, 2771
- Zoccali M., Hill V., Lecureur A., Barbuy B., Renzini A., Minniti D., Gomez A., Ortolani S., 2008, *ArXiv e-prints*, 805
- Zoccali M., Renzini A., Ortolani S., Greggio L., Saviane I., Cassisi S., Rejkuba M., Barbuy B., Rich R. M., Bica E., 2003, *A&A*, 399, 931
- Zucker D. B., Belokurov V., Evans N. W., Kleyna J. T., Irwin M. J., Wilkinson M. I., Fellhauer M., Bramich D. M., et al. 2006, *ApJ*, 650, L41